catalysts

MDPI

Article

Multimetallic Nano-Oxides as Co-Catalysts of an Fe Molecular Catalyst for Enhanced H_2 Production from HCOOH: Thermodynamic and Nanostructural Insights

Christos Dimitriou [1], Konstantina Gravvani [2], Anastasios Asvestas [3], Dimitrios F. Anagnostopoulos [3], Maria Louloudi [2,*] and Yiannis Deligiannakis [1,*]

[1] Laboratory of Physical Chemistry of Materials & Environment, Department of Physics, University of Ioannina, 45110 Ioannina, Greece
[2] Laboratory of Catalysis and Hybrid Materials, Department of Chemistry, University of Ioannina, 45110 Ioannina, Greece
[3] Department of Material Science and Engineering, University of Ioannina, 45100 Ioannina, Greece
* Correspondence: mlouloud@uoi.gr (M.L.); ideligia@uoi.gr (Y.D.); Tel.: +30-2651008418 (M.L.); +30-2651008662 (Y.D.)

Abstract

Renewable H_2 production emerges as a forward-looking technology towards green energy transition. Herein, we present a study on novel multimetallic nano-oxides used as co-catalysts for H_2 production via HCOOH dehydrogenation (FADH) by an Fe^{II}(Polyphosphine) molecular catalyst, under near-ambient P, T conditions. The co-catalyst nano-oxides consist of multimetallic {LaSrCrFeO} and {LaSrCrFeVO} perovskites, produced by flame spray pyrolysis (FSP) technology. Kinetic catalytic H_2 evolution data show that both {LaSrCrFeO} and {LaSrCrFeVO} significantly boost H_2 via co-catalytic action. Arrhenius analysis reveals that they decrease the rate-limiting activation energy, E_a. Specifically, E_a = 77.4 kJ mol^{-1} of $\{Fe^{2+}/PP_3\}$ catalyst is decreased to E_a = 67.8 kJ mol^{-1} in {LaSrCrFeO + Fe^{2+}/PP_3} and E_a = 56.2 kJ mol^{-1} in {LaSrCrFeVO + Fe^{2+}/PP_3} catalyst. These significant thermodynamic effects are not observed when the simple parental oxides are used. The present findings are discussed in the context of a boosting role {LaSrCrFeO} and {LaSrCrFeVO} to the key catalytic intermediates of the Fe^{II}(Polyphosphine) catalyst. Technology-wise, this work exemplifies a novel strategy for the industrial production of co-catalysts using FSP technology within the in-situ H_2 production landscape.

Keywords: multimetallic perovskites; flame spray pyrolysis; Fe molecular catalysts; H_2 production; formic acid dehydrogenation

Check for updates

Academic Editor: Antonella Glisenti

Received: 27 November 2025
Revised: 17 December 2025
Accepted: 25 December 2025
Published: 1 January 2026

Copyright: © 2026 by the authors. Licensee MDPI, Basel, Switzerland. This article is an open access article distributed under the terms and conditions of the Creative Commons Attribution (CC BY) license.

1. Introduction

Demand for carbon-neutral energy has intensified research into efficient H_2 carriers that enable safe hydrogen storage and release [1,2]. While H_2 is known for its high energy density and the fact that its utilization—whether as a combustible fuel or in fuel cells—produces only H_2O, its widespread use as a commodity is still hindered by the technical challenges associated with compression, liquefaction, and transportation [3,4]. Liquid organic hydrogen carriers (LOHCs) could address these limitations by enabling the chemical storage of hydrogen rather than gaseous compression, in stable and easy-to-handle liquid media that are compatible with existing fuel infrastructure [5]. Among LOHCs, formic acid (HCOOH) stands as highly promising, due to its favourable thermodynamic properties, high volumetric hydrogen content, and capacity to release H_2 and CO_2 under mild,

catalyst-mediated conditions, without undesirable CO formation [6]. Recent progress in both molecular and supported-metal catalysts demonstrates that, by adjusting the electronic properties of the metal centre, modifying ligand basicity and engineering support-surface functionalities can promote critical intermediates and improve activity [7,8].

In this context, catalytic dehydrogenation of formic acid (FADH) has gained momentum over the last decade as a H_2 production technology operating under near-ambient pressure and temperature conditions (P = 1 atm, T < 100 °C). Specifically, "hybrid" catalytic systems, which integrate well-defined molecular catalysts with solid co-catalysts, have been developed. We previously demonstrated that an Fe^{II} complex with tetra-PHOS ligand PP_3 (Fe^{II}–PP_3), first introduced by Beller et al. [9], functions as a versatile FADH catalyst that can be significantly boosted by grafted nanoparticle ligands [10–15] or co-catalytic materials, such as SiO_2 nanoparticles [16–20]. The mechanistic role of these materials has been comprehensively studied, establishing that they act as genuine co-catalysts rather than sacrificial additives. In particular, their beneficial effect originates from a thermodynamic lowering of the activation energy of the rate-limiting step by ΔE_a = 16–36 kJ mol^{-1} [19]. As an example, one can point to the use of high-surface-area silica (Ox-50 SiO_2) afforded a turnover frequency (TOF) of 13,882 h^{-1} [18], with the enhancement attributed to the presence of surface Si–O–Si bridges that facilitate the formation of the $HCOO^-$ intermediate. Alternatively, replacing bare SiO_2 with imidazole- or amino-functionalized SiO_2 particles, designed as hybrid co-catalysts, led to a further increase in catalytic activity [17–19]. This improvement is assigned to the incorporation of the basic functionalities which enhance formic acid deprotonation and facilitate formate coordination to the metal centre, thereby improving the overall FADH performance [17–19].

Building on this concept, in 2023 we proposed plasmonic nanostructures, specifically Ag@SiO_2 core@shell particles, to function as plasmonic-assisted co-catalysts [21]. Under visible-light irradiation, these materials further promote H_2 evolution in the Fe^{2+}/PP_3 catalytic system through hot-electron transfer. Thus far, our studies have introduced two primary strategies through which co-catalysts can accelerate FADH: (i) enhancement of HCOOH deprotonation at functionalized interfaces, and (ii) electronic modulation of the reaction via the incorporation of nanoplasmonic structures. Both strategies shift the solution potential of the reaction toward more negative values [21,22].

Despite this progress, the full generality of the co-catalytic boosting effect remains to be further explored, i.e., from simple oxides (e.g., SiO_2) to more advanced multimetallic oxides. Hereafter, we put forward the working hypothesis that multimetallic nano-oxides with rich surface chemistry can provide a more versatile platform for developing FADH-enhancing technologies (Figure 1). To this end, we investigated multimetallic perovskite-type oxides, which are known for their tuneable surface acid–base and redox properties [23], as well as their variable oxygen-lattice mobility [24].

The catalytic potential of perovskite-type oxides was recognized as early as the 1970s, when Voorhoeve et al. (1977) demonstrated their structural adaptability and catalytic diversity across oxidation and reduction reactions [25]. Since then, perovskite oxides have been extensively investigated in processes ranging from oxidation catalysis to fuel cell electrodes and photocatalytic H_2 production from H_2O splitting and photocatalytic CO_2 reduction [26–31]. Multimetallic perovskites, incorporating multiple cations at either or both lattice sites, can manifest cooperative effects among redox-active centres, yielding diverse surface coordination environments. Multimetallic perovskites bear conceptual relevance to high-entropy alloys (HEAs) [32–35], which were introduced by Yeh et al. [36] and Cantor et al. [37] in 2004. HEAs incorporate five or more principal metallic elements in near-equimolar ratios, forming single-phase solid solutions wherein the configurational entropy term (ΔS_{config} = R ln N, with N $\geq$ 5) counterbalances positive mixing enthalpy,

thereby suppressing phase segregation. Building on this paradigm, Rost et al. (2015) extended the concept to oxides, reporting the first high-entropy oxide (HEO)—in the rocksalt (MgCoNiCuZn)O system [38]. In such systems, five or more cations randomly occupy a crystallographic sublattice, generating configurational entropies of approximately $\Delta S_{config} = 1.61$ R ($\sim$13.4 J mol^{-1} K^{-1}) for quinary equimolar compositions [39,40]. This entropic contribution stabilizes single-phase structures and imparts thermal stability, defect tolerance, and tuneable redox behaviour—attributes that underpin the emergence of HEOs as functional catalysts and electrocatalysts.

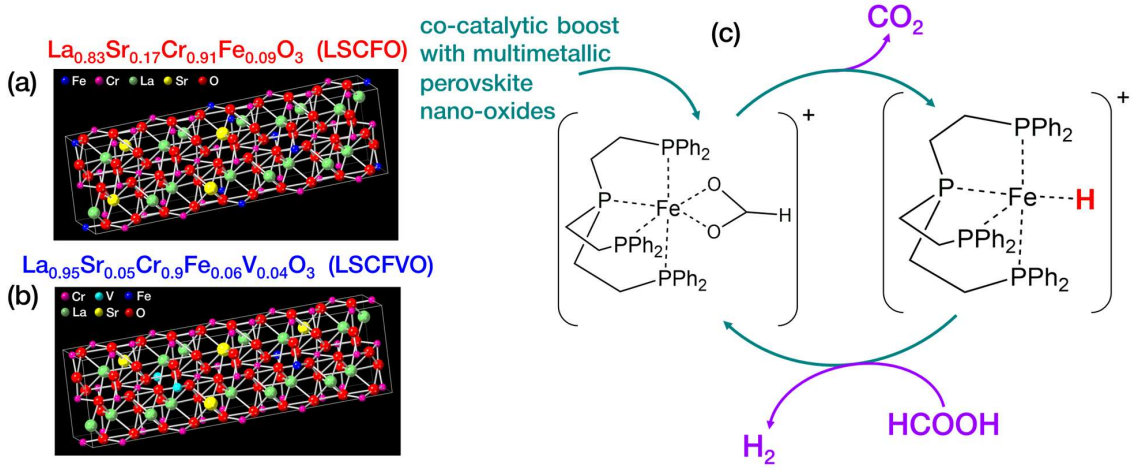


Figure 1. Visualization of the crystal structures of (**a**) LSCFO and (**b**) LSCFVO multimetallic perovskite materials, generated using CrystalMaker software (Version 11). The models illustrate the cation arrangement within the perovskite lattice and the distribution of A- and B-site dopants. (**c**) Involvement of multimetallic perovskite oxides in the catalytic formic acid dehydrogenation mechanism, using the Fe^{2+}/PP_3 molecular catalyst.

To broaden this framework beyond strictly equimolar compositions, Wright and Luo (2020) introduced the concept of compositionally complex ceramics (CCCs) [41], later extended by Brahlek et al. (2022) to compositionally complex oxides (CCOs) [42–44]. This taxonomy distinguishes CCOs from classical HEOs and entropy-stabilized oxides (ESOs), encompassing systems that exhibit high cationic diversity without the strict equimolar or entropy thresholds of HEOs.

Accordingly herein, we have synthesized two multimetallic perovskites—$La_{0.75}Sr_{0.25}Cr_{0.9}Fe_{0.1}O_{3-\delta}$ and $La_{0.75}Sr_{0.25}Cr_{0.9}Fe_{0.05}V_{0.05}O_{3-\delta}$ (see Figure 1a)—that reside in the *medium-entropy oxide* (MEO) regime [45–47]. Their non-equimolar distributions and three B-site metals (Cr, Fe, V) yield configurational entropies below the ~1.61 R threshold typical of HEOs yet significantly higher than those of conventional doped perovskites. Thus, these MEO perovskites bridge traditional doped oxides and true high-entropy systems, combining enhanced cationic diversity with structural and functional tunability. Similar MEO-perovskite nano-oxides as cathodes have been used in intermediate-temperature solid oxide fuel cells (IT-SOFCs) for oxygen reduction [48] and in solid oxide electrolysis cells (SOECs) for H_2O/CO_2 electrolysis, employing either Ce-doped [49] or {LaSrCrFeO} [50,51] perovskites to enhance redox stability and catalytic activity.

The synthesis method plays a decisive role in determining structural and electronic order. Recently, we have exemplified the development and optimization of flame spray pyrolysis (FSP) as an industrial-scale method for the synthesis of perovskite oxides, including bismuth ferrite ($BiFeO_3$) and sodium tantalate ($NaTaO_3$) [52–54]. The rapid heating and quenching intrinsic to FSP promote metastable cation distributions, nanoscale lattice strain, and defect incorporation [55–58]. So far, Phakatkar et al. have reported FSP synthesis of homogeneous, single-phase (Mn, Fe, Ni, Cu, Zn)$_3O_4$ high-entropy oxide nanoparti-

cles, elucidating how rapid quenching stabilizes multicomponent cation distributions and defect-rich spinel lattices [59]. In the work of Dai and co-workers [60], a quinary ultra-small HEA of {PtPdIrRuRh} supported on TiO_2 was synthesized via FSP, exhibiting outstanding CO_2 hydrogenation performance. Zheng et al. developed a one-step FSP method to synthesize high-entropy oxide Pt@$(CrMnFeCoNi)_3O_4$ core–shell nanoparticles, which exhibited enhanced catalytic activity and a lower light-off temperature for CO oxidation [61]. Luo et al. synthesized single-phase spinel $(FeCoNiCrMn)_3O_4$ HEO nanoparticles via FSP with controlled ultrafast air quenching, demonstrating that lattice-strain engineering through rapid cooling enhances oxygen vacancy formation and significantly improves oxygen evolution reaction (OER) activity [56].

Herein, we use FSP to prepare the two types of multimetallic perovskites (see also the structure σ in Figure 1a), as follows:

$$A_{1-x}A'_xB_{1-y}B'_yO_3: \ La_xSr_xCr_{1-y}Fe_yO_3 \quad (1)$$

$$A_{1-x}A'_xB_{1-y-z}B'_yB''_zO_3: \ La_xSr_xCr_{1-y}Fe_yV_zO_3 \quad (2)$$

Our working hypothesis was that A-site substitution (La/Sr) could modulate lattice parameters, oxygen vacancy formation energies, and charge compensation mechanisms, thereby influencing B-site redox flexibility. At the B-site, Cr, Fe, and V can access multiple oxidation states (Cr^{3+}/Cr^{4+}, Fe^{3+}/Fe^{4+}, V^{4+}/V^{5+}), providing redox-active centres capable of mediating electrons and affecting the solution potential of FADH. Thus, our goal was to elucidate the role of such MEOs as co-catalysts for the Fe^{2+}/PP_3 system in H_2 production from HCOOH (Figure 1).

The specific aims were [a] to develop and optimize an FSP synthesis protocol for controlled preparation of La–Sr–Cr–Fe and La–Sr–Cr–Fe–V as medium-entropy perovskites; [b] to validate their role as co-catalysts for FADH/H_2 generation by the benchmark Fe^{2+}/PP_3 molecular catalyst under near-ambient pressure and temperature conditions (P = 1 atm, T < 100 °C); and [c] to analyse the thermodynamic basis of the observed co-catalytic enhancement, activation energy, and solution potential elucidating how lattice strain influences the catalytic processes.

2. Results and Discussion

2.1. FSP Engineering of Multimetallic Perovskite Nano–Oxides

X-Ray Diffraction: Figure 2a presents the XRD patterns of the as-prepared multimetallic perovskite nano-oxides produced via flame spray pyrolysis (FSP). The crystallographic phases have been identified and are indicated with vertical coloured reference lines in Figure 2a and are summarized in Table 1.

Table 1. FSP-prepared multimetallic perovskites and their structural parameters.

Material	FSP Nominal Configuration	Crystallographic Phase (XRD, PDF)	XRF-Determined Stoichiometry	d_{XRD} (nm) (±0.5)	SSA (m^2 gr^{-1}) (±1)	Pore Volume (cm^3 gr^{-1}) (±0.005)
As-prepared						
LSCFO	$La_{0.75}Sr_{0.25}Cr_{0.9}Fe_{0.1}O_{3-\delta}$	$La_{0.9}Sr_{0.1}Cr_{0.8}Fe_{0.2}O_3$	$La_{0.83}Sr_{0.17}Cr_{0.91}Fe_{0.09}O_3$	65	11	0.073
LSCFVO	$La_{0.75}Sr_{0.25}Cr_{0.9}Fe_{0.05}V_{0.05}O_{3-\delta}$		$La_{0.95}Sr_{0.05}Cr_{0.9}Fe_{0.06}V_{0.04}O_3$	75	13	0.096
LSO	$La_{0.75}Sr_{0.25}O_{3-\delta}$	90% La_2O_3 + 10% La-Sr-O	$La_{0.88}Sr_{0.12}O_3$	50	12	0.043
CFO	$Cr_{0.9}Fe_{0.1}O_{3-\delta}$	Cr_2O_3	$Cr_{0.91}Fe_{0.09}O_3$	40	37	0.261
Post-FSP treated						
LSCFO-c	LSCFO calcined at 400 °C for 2h in air	$La_{0.9}Sr_{0.1}Cr_{0.8}Fe_{0.2}O_3$	–	65	–	–
LSCFVO-c	LSCFVO calcined at 400 °C for 2h in air		–	76	–	–

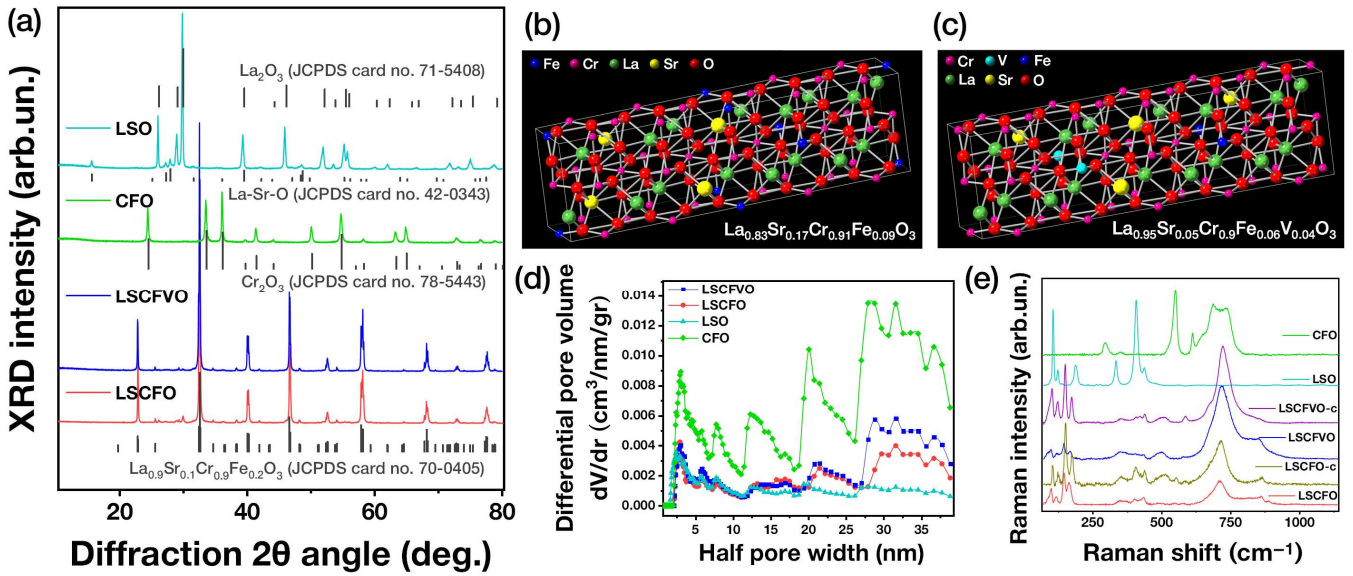


Figure 2. (**a**) XRD patterns of the investigated multimetallic perovskite nano-oxides (LSCFO and LSCFVO) and the single-site doped oxides (LSO and CFO), together with the corresponding JCPDS reference patterns. (**b**,**c**) CrystalMaker visualizations of the multimetallic perovskites (**b**) LSCFO and (**c**) LSCFVO, constructed using the experimentally determined stoichiometries obtained from XRF spectroscopy. (**d**) Pore size distribution plot using the DFT method for the studied materials. (**e**) Raman spectra of the multimetallic perovskites LSCFO and LSCFVO, examined both in their as-prepared form and after calcination at 400 °C for 2 h (denoted LSCFO-c and LSCFVO-c, respectively), along with the single-site doped oxides LSO and CFO.

In the single-site doped oxides {LaSrO} and {CrFeO}, namely LSO and CFO, the partial substitution of La and Cr by Sr (x = 0.25) and Fe (y = 0.1) represents a relatively low doping level. Our XRD data (Figure 2a, green and cyan lines) show that their crystallographic phases correspond to the respective mono-oxides: lanthanum oxide (La_2O_3) for LSO and chromium oxide (Cr_2O_3) for CFO. La_2O_3 crystallizes in the hexagonal (A-type) structure (space group $P6_3/mmc$, JCPDS No. 71-5408), with lattice parameters $a = b = 3.94$ Å and $c = 6.13$ Å, while the Cr_2O_3 phase is indexed to a rhombohedral (corundum-type) structure (space group $R\bar{3}c$, JCPDS No. 78-5443), which can also be represented in the equivalent hexagonal setting with lattice parameters $a = b = 4.96$ Å and $c = 13.59$ Å. In addition to the LSO material, a weak and broad diffraction pattern corresponding to a La–Sr–O framework was observed, which qualitatively matches the low-precision JCPDS card No. 42-0343 (see Figure 2a, yellow vertical lines). This pattern likely represents a non-stoichiometric La–Sr–O oxide or partially amorphous intermediate phase formed under our FSP process, rather than a well-defined crystalline compound. Therefore, the La–Sr–O contribution is interpreted as a structural framework indicative of La–Sr interaction. In contrast, no distinct Cr–Fe–O diffraction features were detected in the XRD pattern of CFO, likely due to the lower dopant concentration relative to the La/Sr system. Using the Scherrer equation (Equation (3)), the crystallite sizes were estimated from the XRD peak with Miller indices [0 1 1] at 2θ = 29.9° for LSO, yielding 50 nm, and from the [1 0 4] peak at 2θ = 33.6° for CFO, resulting in 40 nm, listed in Table 1. These values are consistent with the nanoscale domain dimensions typically observed in FSP-derived oxide materials [57,62].

For the multimetallic perovskite LSCFO, the XRD pattern shows a single-phase structure (see Figure 2a, red line), as evidenced by the identified crystallographic phase indicating that all constituent metals were successfully incorporated. Specifically, the $La_{0.9}Sr_{0.1}Cr_{0.8}Fe_{0.2}O_3$ phase is indexed to an orthorhombic perovskite structure (space group *Pnma*, JCPDS No. 70-0405), with lattice parameters $a = 5.486$ Å, $b = 7.765$ Å, and

c = 5.523 Å (V = 235.3 Å^3, Z = 4). This phase belongs to the distorted orthorhombic family of La–Sr–Cr–Fe perovskites, consistent with B-site mixed occupancy and partial A-site Sr substitution. A minor secondary phase (<2%) at 25–30° corresponding to La_2O_3 was detected, likely originating from a small fraction of lanthanum that was not incorporated into the perovskite lattice. The low intensity of these peaks is consistent with their trace contribution and is in agreement with the XRF results (see Table S1), which indicate a slight excess of La relative to the nominal perovskite stoichiometry. Given the very low fraction of secondary phases, the absence of phase segregation at the macroscale, and the fact that the primary focus of this work is catalytic performance rather than detailed crystallographic modelling, we consider that full XRD refinement would not provide additional physically meaningful insight within the scope of the present study.

From the XRD data of the LSCFVO material (Figure 2a, blue line), we identified the same crystallographic phase as $La_{0.9}Sr_{0.1}Cr_{0.8}Fe_{0.2}O_3$, with no distinct vanadium-containing phase detected. To our knowledge, no reference pattern or database entry exists for a single-phase perovskite containing all five metals (La, Sr, Cr, Fe, and V). In this sample, a trace secondary phase of La_2O_3 (<1%) was also observed. Similarly, using the XRD peak [*h k l*] = [1 2 1] at 2θ = 32.5° for both LSCFO and LSCFVO, the crystallite sizes were estimated to be 65 nm and 75 nm, respectively, as listed in Table 1. The larger particle sizes compared with the single-site doped materials (LSO and CFO) indicate that the crystallite growth proceeds more extensively in the high-temperature regime of FSP, as the incorporation of multiple cations (four or five metals per unit cell) increases the unit cell volume. This also explains why LSCFVO, which contains five metals (La, Sr, Cr, Fe, and V), exhibits the largest crystallite size within the series, reflecting its more complex multi-cation environment.

XRF Spectroscopy: All studied materials—namely the multimetallic perovskites LSCFO and LSCFVO, as well as the single-site doped oxides LSO and CFO—were analysed using X-ray fluorescence (XRF) spectroscopy (Figure S1). The corresponding XRF spectra are shown in Figure S1. The measured metal weight percentages (w/w %) for each sample are summarized in Table S1 of the Supporting Information. The XRF quantification reveals that the experimentally obtained cation stoichiometries exhibit only minor deviations from the nominal target compositions. In Figure S1c, the V Kα emission line is highlighted for comparison between the LSCFO and LSCFVO materials. Because V is present at a very low concentration (1.1 w/w %), its signal is inherently weak and difficult to detect. In our spectra, the V Kα contribution manifests primarily as a subtle broadening on the left side of the adjacent La Lβ peak, which is consistent with observations reported in the literature for low-level V incorporation [63]. A pronounced decrease is observed only for Sr relative to the other metals. This behaviour is expected, as Sr^{2+} is the largest cation among the constituent elements (based on Shannon ionic radii: $Sr^{2+} > La^{3+} > Fe^{3+} > Cr^{3+} > V^{5+}$), and numerous studies report that Sr incorporation into perovskite lattices is intrinsically challenging. In addition, we suspect that the pH of the precursor solution may promote partial Sr precipitation, further reducing the available Sr content for lattice incorporation.

As shown by the XRF data (Figure S1 and Table S1), both the single-site doped oxide (LSO) and the multimetallic perovskite (LSCFO) exhibit a 35–50% reduction in Sr relative to the nominal value. In contrast, for LSCFVO, where five different cations must be simultaneously accommodated within a single perovskite lattice, the Sr under-incorporation reaches ∼80%. This substantial decrease suggests that increasing compositional complexity intensifies competition for lattice sites and further suppresses Sr incorporation.

Overall, based on the combined XRD and XRF data (Tables 1 and S1), the crystal structures of the LSCFO and LSCFVO materials were visualized using the CrystalMaker software. As no standard crystal structure for this material exists in the literature or crys-

tallographic databases, the modelling was initiated from the known $LaCrO_3$ perovskite structure, as La and Cr are the predominant A- and B-site cations, respectively. $LaCrO_3$ crystallizes in an orthorhombically distorted perovskite structure (space group *Pnma*, No. 62), with lattice parameters a = 5.478 Å, b = 7.758 Å, and c = 5.501 Å [64]. The distortion arises from cooperative tilting of the CrO_6 octahedra due to the relatively small A-site cation (La^{3+}). This structure type was selected as the reference framework in CrystalMaker, from which the partially substituted LSCFO and LSCFVO models were constructed by replacing La with Sr at the A-site and introducing Fe (and V) at the B-site positions according to the experimental stoichiometries. To visually represent the small substitutional fractions of Sr, Fe, and V within the perovskite lattice, the primitive unit cell was expanded into a 5 × 1 × 1 supercell, see Figure 2b,c. This approach allowed the dopant atoms to be distributed in a realistic spatial configuration, enabling a clearer visualization of their incorporation into the La–Sr–Cr–Fe and La–Sr–Cr–Fe–V frameworks.

Raman Spectroscopy: Figure 2e displays the Raman spectra of multimetallic perovskites LSCFO and LSCFVO, the single-site doped oxides (LSO, CFO), as well as the corresponding calcined samples (LSCFO-c, LSCFVO-c). For the four as-prepared nanomaterials, we successfully assigned all vibrational bands, which are summarized in Table S2 of the Supporting Information. Beginning with LSO {LaSrO}, the vibrational peaks at 106 [E_g], 124 [E_g/A_{1g}], 188 [A_{1g}], 335 [E_g], and 408 [A_{1g}] cm^{-1} correspond to characteristic La_2O_3 lattice modes [65–67]. Small shifts in these bands can be interpreted as strain- or disorder-induced distortions arising from the incorporation of Sr into the La_2O_3 framework. Additionally, the feature at 437 [E_g] cm^{-1} is attributed to Sr-induced A-site disorder, which introduces local structural perturbations that likely activate this shoulder mode [65–67]. Regarding the CFO {CrFeO} material, the vibrational modes at 298 [E_g], 351 [E_g], 550 [A_{1g}] and 612 [E_g] cm^{-1} are consistent with the characteristic lattice modes of α-Cr_2O_3 reported in the literature [68–70]. However, the bands observed at 687 and 740 cm^{-1} do not correspond to the established chromium-oxide phonon framework and are more plausibly assigned to defect-activated local modes arising from Fe incorporation into the α-Cr_2O_3 corundum lattice [68–70]. For the LSCFO {LaSrCrFeO} multimetallic perovskite nano-oxide, the low-frequency region (99 [A_g], 118 [B_{2g}], 146 [A_g/B_g], 165 [A_g/B_{2g}] cm^{-1}) is dominated by A-site (La/Sr) vibrational modes coupled with octahedral tilting, characteristic of the external phonon modes of *Pnma*-type $LaCrO_3$ [71–73]. The mid-frequency bands (360 [B_{2g}/B_{3g}], 402 [A_g], and 436 [A_g] cm^{-1}) correspond to O–Cr–O bending and rotation modes of the CrO_6 framework, whose small shifts relative to undoped $LaCrO_3$ reflect lattice distortions induced by Sr/Fe substitution [70–75]. At higher wavenumbers (711 [A_g] cm^{-1}), a broad defect-activated Cr/Fe–O stretching mode appears, consistent with Sr/Fe-driven local disorder and oxygen non-stoichiometry [73]. Weak bands near 860–890 cm^{-1} are attributed to trace chromate-type surface phases at grain boundaries, commonly reported in La–Cr–O and Sr–Cr–O systems [76,77]. Lastly, for LSCFVO material, the Raman spectrum remains dominated by $LaCrO_3$-type modes, reflecting the La/Sr A-site framework and the Cr/Fe/V B-site lattice. The low-frequency region (98 [A_g], 120 [B_{2g}], 146 [A_g/B_g], 169 [A_g/B_{2g}] cm^{-1}) is governed by A-site (La/Sr) vibrations coupled with octahedral tilting of *Pnma* perovskites [71–73]. Mid-frequency features (353 [B_{2g}/B_{3g}], 435 [A_g], 499 [A_g/A_g] cm^{-1}) arise from O–(Cr/Fe/V)–O bending and rotation modes of the mixed B-siteO_6 octahedra, with the small shifts relative to $LaCrO_3$ indicating lattice distortion from Sr/Fe/V substitution [71,73,78,79]. A defect-activated band near ~720 [A_g] cm^{-1} reflects oxygen-vacancy-related local distortions of (Cr/Fe/V)O_6 octahedra [73]. The high-frequency peak at 853 [A_g] cm^{-1} is assigned to symmetric V–O stretching of VO_4-type units associated with minor surface vanadate species [80–82].

N_2 Porosimetry: To further understand the lattice structure, the N_2 adsorption isotherms for the FSP-made multimetallic nanomaterials are presented in Figure S2. All nanomaterials have the characteristics of a type-IV isotherm. The SSA values and pore volume analysis show that for LSO and LSCFO/LSCFVO, the specific surface areas are relatively low (11–13 m^2 gr^{-1}), whereas CFO exhibits higher SSA of 37 m^2 gr^{-1}, as listed in Table 1. This increase is consistent with the XRD results, as CFO possesses the smallest crystallite size. Smaller primary crystallites generated during FSP produce a larger external surface area and yield more finely divided aggregates [57,58], thereby explaining the substantially higher SSA of the CFO sample. Beyond crystallite-size effects, this behaviour can also be rationalized by the intrinsic properties of the constituent atoms. CFO consists exclusively of transition-metal cations (Cr and Fe), which form highly refractory, high-melting point oxides that resist sintering and coalescence in the FSP flame, favouring the formation of very small primary particles [83]. In contrast, the La- and Sr-containing oxides incorporate heavier, more polarizable A-site cations, which promote enhanced surface mobility and partial densification during particle formation, yielding coarser aggregates with lower SSA [84]. These combined effects—smaller crystallite size and reduced sintering—explain the markedly higher SSA observed for CFO compared with the La-based oxides.

An analogous interpretation is obtained from the pore volume analysis, which follows the trend LSO < LSCFO < LSCFVO $\ll$ CFO, as shown in Table 1 and Figure 2d. CFO exhibits the highest pore volume (0.261 cm^3 gr^{-1}), consistent with the formation of highly open Cr–Fe–O aggregates with limited sintering during FSP, which results in a large interparticle void fraction. In contrast, the LSO sample shows the lowest pore volume (0.043 cm^3 gr^{-1}), in agreement with the behaviour of a $La_2O_3/LaSrO_x$ framework that undergoes more extensive coarsening and partial densification during FSP, producing relatively compact aggregates with minimal accessible porosity. The multimetallic perovskites LSCFO and LSCFVO exhibit intermediate pore volumes (0.073 and 0.096 cm^3 gr^{-1}, respectively). Their larger values relative to LSO reflect the more open aggregate structure of the La/Sr–Cr/Fe(–V) perovskite network compared with the denser La-based oxide. The modest increase observed upon V incorporation in LSCFVO indicates additional structural/compositional disorder and inhibited densification of the mixed $(Cr/Fe/V)O_6$ framework during FSP.

Thermogravimetric Analysis: The thermogravimetric profiles of the multimetallic perovskites LSCFO and LSCFVO (see Figure S3) reveal only minimal mass variations, confirming their excellent thermal stability after flame spray pyrolysis. In LSCFO, a small mass decrease of approximately 0.2% is observed below 300 °C, which is attributed to the removal of physiosorbed water and the combustion of trace organics remaining from precursor decomposition in the flame. At higher temperatures, after 350 °C, the material exhibits a slight mass gain of about 0.3%. This increase reflects a moderate uptake of oxygen, consistent with the oxidation of minor oxygen-deficient regions within the Cr–Fe perovskite lattice and the progressive structural rearrangement toward a more ordered crystalline framework. The LSCFVO sample displays qualitatively similar behaviour but with much smaller mass loss at low temperatures and a larger mass gain at elevated temperatures. The absence of a pronounced initial weight decrease suggests more complete combustion of volatile species during FSP. At higher temperatures, LSCFVO undergoes a measurable mass increase of roughly 0.8%, significantly higher than that of LSCFO. This enhancement is attributed to the oxygen uptake associated with the oxidation of the mixed $(Cr/Fe/V)O_6$ octahedral network, particularly the conversion of V^{3+}-containing environments toward higher valence states (e.g., V^{5+}), and to the filling of oxygen vacancies generated during rapid nanoparticle formation. The stronger thermal feature in the TG curve supports the presence of more pronounced lattice reorganization and defect equilibration in the

vanadium-containing perovskite. Overall, the TGA results indicate that both materials are structurally stable as synthesized, with only minor thermal events related to dehydration, oxidation, and crystallographic refinement.

2.2. Catalytic H_2 Production from HCOOH: Multimetallic Perovskites as Co–Catalysts

The H_2/FADH data are presented in Figure 3. It is seen that addition of the multimetallic perovskites significantly enhances the catalytic performance of the Fe^{2+}/PP_3 system in FADH. Specifically, the data in Figure 3a show that the gas evolution profiles showed that, while the Fe^{2+}/PP_3 catalyst alone produced 1900 mL of [H_2 + CO_2] after 90 min, the addition of LSCFO and LSCFVO markedly accelerated the reaction, producing the same gas volume within 35–40 min.

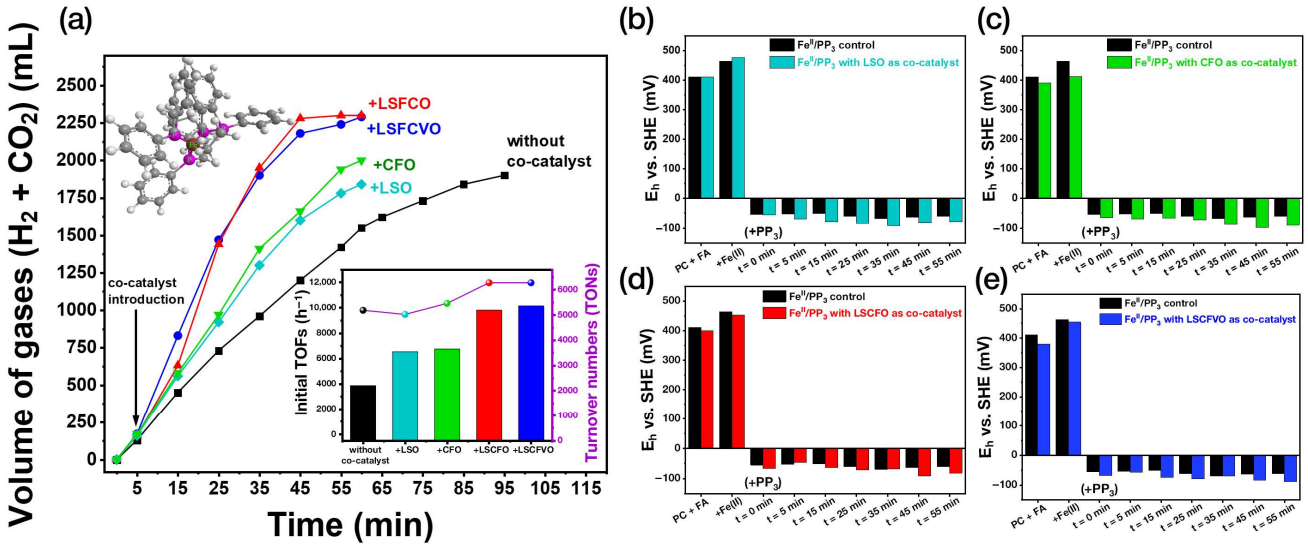


Figure 3. (**a**) Volume of gas evolved by the Fe^{2+}/PP_3 catalytic system in the absence (black line) and in the presence of LSO (cyan line), CFO (green line), LSCFO (red line), and LSCFVO (blue line); *inset:* initial TOFs and turnover numbers of the Fe^{2+}/PP_3 system with or without co-catalyst addition during FADH. Additionally, the 3D structure represents the Fe^{2+}/PP_3 system. (**b**–**e**) Comparative E_h profiles of {Fe^{2+}/PP_3} control (black bars) and (**b**) {LSO + Fe^{2+}/PP_3}, (**c**) {CFO + Fe^{2+}/PP_3}, (**d**) {LSCFO + Fe^{2+}/PP_3}, and (**e**) {LSCFVO + Fe^{2+}/PP_3} catalysts. Catalytic conditions: PC/FA solution (4/2 *v*/*v*) T = 80 °C (±1 °C), followed by the addition of 7.5 μmol Fe^{2+} precursor ($Fe(BF_4)_2 \cdot 6H_2O$) (2.5 mg) and 7.5 μmol PP_3 phosphine (5 mg), 10 mg of co-catalyst (pre-dispersed in 1 mL of PC) was introduced in the reaction solution after 5 min.

The TOFs and total turnover numbers (TONs) (Figure 3a, inset) confirm the boosting effect. Specifically, the Fe^{2+}/PP_3 control system exhibited TOF of ~3900 h^{-1} and TONs > 5000, whereas {LSCFO + Fe^{2+}/PP_3} and {LSCFVO + Fe^{2+}/PP_3} nearly tripled the initial TOF values (9800–10,000 h^{-1}) and increased the TONs to >6000. Interestingly the simple oxides CFO and LSO showed a much lower H_2/FADH boosting i.e., {CFO + Fe^{2+}/PP_3} showed a moderate enhancement, with an initial rate of 41 mL min^{-1} (initial TOF ~ 6800 h^{-1}). Likewise, {LSO + Fe^{2+}/PP_3} provided a comparable co-catalytic contribution in the {Fe^{2+}/PP_3} homogeneous system, giving an initial rate of 40 mL min^{-1} (initial TOF > 6500 h^{-1}). For completeness we draw attention to the fact that the purity of the catalytic materials might affect/inhibit the H_2/FADH, e.g., a chloride-contaminated LSO (Cl-LSO) (see XRF data in Figure S4), due to Cl leftovers from the FSP process, had a deleterious effect on the H_2/FADH {Fe^{2+}/PP_3}, as shown in Figure S5a. In contrast, the high-purity FSP-made materials were appropriate H_2/FADH boosters.

Overall, the present data clearly demonstrate the distinct beneficial role of the high-purity multimetallic LSCFVO and LSCFO oxides as co-catalysts for FADH catalysed by the

{Fe^{2+}/PP_3} under near-ambient pressure and temperature conditions (P = 1 atm, T < 100 °C). The key observation being that CFO and LSO provide only a modest enhancement. This observation reveals that the multimetallic perovskite lattices create unique reaction sites that are not present in the corresponding "parent" single-oxide materials.

2.2.1. The Effect of Co-Catalyst Mass

The influence of the mass of multimetallic perovskite co-catalysts on the Fe^{2+}/PP_3 system was further examined by varying the amount of LSCFO and LSCFVO added to the reaction (Figure S6). As shown in Figure S6a,b, the catalytic H_2/FADH activity of the Fe^{2+}/PP_3 system increased with co-catalyst loading and reached a maximum at 10 mg, yielding a gas evolution rate of 64 mL min^{-1} for both oxides—corresponding to an increase of more than 110% compared with the 30 mL min^{-1} rate of the Fe^{2+}/PP_3 system alone. Beyond 10 mg, additional co-catalyst did not further enhance the rate; instead, a slight decrease was observed. This decline is consistent with the typical behaviour we have observed for other solid co-catalysts [17], where excess particles can hinder mass transport and limit the accessibility of redox-active surface sites. Overall, these results demonstrate that 10 mg represents the optimal mass loading for both LSCFO and LSCFVO, providing an effective balance between surface accessibility and co-catalytic efficiency within the Fe^{2+}/PP_3 catalytic system. Based on the present results, this optimized loading of 10 mg LSCFO or LSCFVO was selected and used throughout all subsequent catalytic studies.

2.2.2. Solution Potential (E_h) Determination

To peer into the factors underlying this observed catalytic H_2/FADH boost, the solution potential (E_h) od the catalytic mixture was monitored [22] continuously. Recently, we demonstrated that the trends in E_h values in FADH systems can provide critical insights into the redox events occurring in the solution during catalysis. Herein, as a reference, prior to the catalytic process, dispersions of the oxides in O_2-free propylene carbonate exhibited the E_h values: LSO, +175 mV; CFO, +305 mV; LSCFO, +318 mV; and LSCFVO, +288 mV. Although all materials displayed oxidizing potentials, these distinct E_h values indicate that each oxide is expected to modify the catalytic microenvironment differently when introduced into the active FA/Fe^{2+}/PP_3 system.

Under catalytic conditions, E_h monitoring was employed to probe changes in the catalytic environment during FADH in the FA/Fe^{2+}/PP_3 catalytic system (Figure 3b–e). Initially, all systems exhibited similar behavior: the solution potential of the PC + FA mixture showed the typical values +400 to +450 mV, then, E_h increased upon addition of the Fe^{2+} precursor, and then dropped sharply to negative values after PP_3 addition, indicating the—well understood—establishment of a strongly reducing environment [10,12,22].

In Figure 3, once the co-catalysts were introduced at $t_{catalysis}$ = 5 min, the E_h-trends of the systems began to diverge: in the control Fe^{2+}/PP_3 (black bars), where no co-catalyst was added, E_h was stabilized at moderately negative values (−55 to −70 mV), which remained stable over time. In contrast, addition of LSO (Figure 3b), CFO (Figure 3c), LSCFO (Figure 3c) or LSCFVO (Figure 3d) in Fe^{2+}/PP_3 resulted in progressively more negative E_h values, typically −70 to −100 mV, which remained—generally—steady, with some fluctuations, throughout the reaction. As we have reported previously [10,12,22], this sustained reducing E_h, in any case, reflects the ability of the multimetallic perovskites to facilitate key-intermediate species for efficient FADH catalysis and confirms catalytic results.

For completeness, the Cl-contaminated LSO {Cl-LSO + Fe^{2+}/PP_3} was unable to maintain a reducing environment; the E_h rapidly increased to values above +200 mV, indicating a strongly oxidizing medium (Figure S5b). This shift is consistent with catalyst deactivation rather than co-catalytic promotion.

2.2.3. Evaluation of Thermally-Treated Co-Catalysts

To further understand the role of surface properties on the observed H_2/FADH boost, a moderate thermal treatment (400 °C for 2 h, under air) was applied. For the {LaSrCrFeO} perovskite (Figure S7a, inset), the as-prepared {LSCFO + Fe^{2+}/PP_3} exhibited the highest activity, whereas its calcined counterpart {LSCFO-c + Fe^{2+}/PP_3} still produced a pronounced enhancement vs. Fe^{2+}/PP_3 alone. Notably, the E_h profile of {LSCFO-c + Fe^{2+}/PP_3} remained substantially more negative than that of the control throughout the reaction, (Figure S7a), demonstrating that calcination does not abolish the co-catalytic functionality required to promote FADH. Rather, the slightly attenuated rate (51 mL min^{-1} compared with 64 mL min^{-1}) suggests a modification or partial restructuring of the active surface sites upon thermal treatment.

A similar trend was observed for {LaSrCrFeVO} (Figure S7b, inset). The as-prepared {LSCFVO + Fe^{2+}/PP_3} generated the highest initial H_2 rate among all materials tested (65 mL min^{-1}), while its calcined analogue {LSCFO-c + Fe^{2+}/PP_3} remained active, exhibiting a comparable gas-production rate (61 mL min^{-1} vs. 30 mL min^{-1} of Fe^{2+}/PP_3) and an E_h profile that clearly surpassed the Fe^{2+}/PP_3. The ability of {LSCFO + Fe^{2+}/PP_3} to maintain more negative E_h values throughout the reaction (Figure S7b) indicates that the multimetallic oxide framework preserves efficient co-catalytic activity pathways even after thermal treatment.

Overall, although the moderate-calcination slightly decreased the H_2/FADH activity—likely due to modifications in surface area and/or lattice strain—their persistently negative E_h values and enhanced catalytic kinetics confirm that the essential co-catalytic interface between the {FA/Fe^{2+}/PP_3} system and the perovskite lattice remains largely intact.

Taken together, the present H_2 production results and the corresponding E_h trends conclusively indicate that:

[i] In the {LSCFO + Fe^{2+}/PP_3} and {LSCFVO + Fe^{2+}/PP_3} systems, the multimetallic perovskites act as efficient co-catalysts, significantly enhancing the FADH rates under near-ambient pressure and temperature conditions (P = 1 atm, T < 100 °C).

[ii] These systems generate a more reducing environment, as evidenced by their lower E_h values.

[iii] This beneficial role is observed exclusively for LSCFO and LSCFVO; in contrast, the parent oxides LSO and CFO are not as effective, and Cl-LSO may even exert a poison effect.

2.3. Thermodynamic Arrhenius Analysis

To gain deeper insight into the physicochemical role of the multimetallic nano-oxides and given that FADH is a thermally activated process, we performed a temperature-dependent kinetic analysis to determine the corresponding activation energies (Figure 4). These values were obtained from Arrhenius plots of the natural logarithm of the TOF versus the inverse temperature (1/T), constructed both in the absence and in the presence of the multimetallic particles.

The control Fe^{2+}/PP_3 catalytic system exhibited an E_a of 77.4 ± 3.1 kJ mol^{-1} (Figure 4a, black line), consistent with previously reported studies [9,18]. Upon introduction of the perovskite-type co-catalysts, a clear and systematic E_a decrease was observed. As analyzed in detail previously [9,18], this E_a-lowering demonstrates that the nano-oxides effectively promote key-intermediate species of FADH catalysis. For the LSCFO (Figure 4a,c, red line), the as-prepared material decreased E_a to 67.8 ± 3.3 kJ mol^{-1}, indicating a substantial enhancement in catalytic efficiency. Moderate calcination at 400 °C (LSCFO-c) achieved a smaller decrease of E_a = 71.5 ± 2.8 kJ mol^{-1} (Figure 4c, gold-colored line), with the ensuing decrease in H_2/FADH performance compared with the FSP as-prepared co-catalyst. This trend—upon thermal treatment—likely indicates that suggests that partial surface

restructuring, e.g., defects, oxygen vacancies, or labile OH, features that typically diminish during thermal treatment, decreased the synergistic interaction between the perovskite-co-catalyst and components of FADH catalysis.

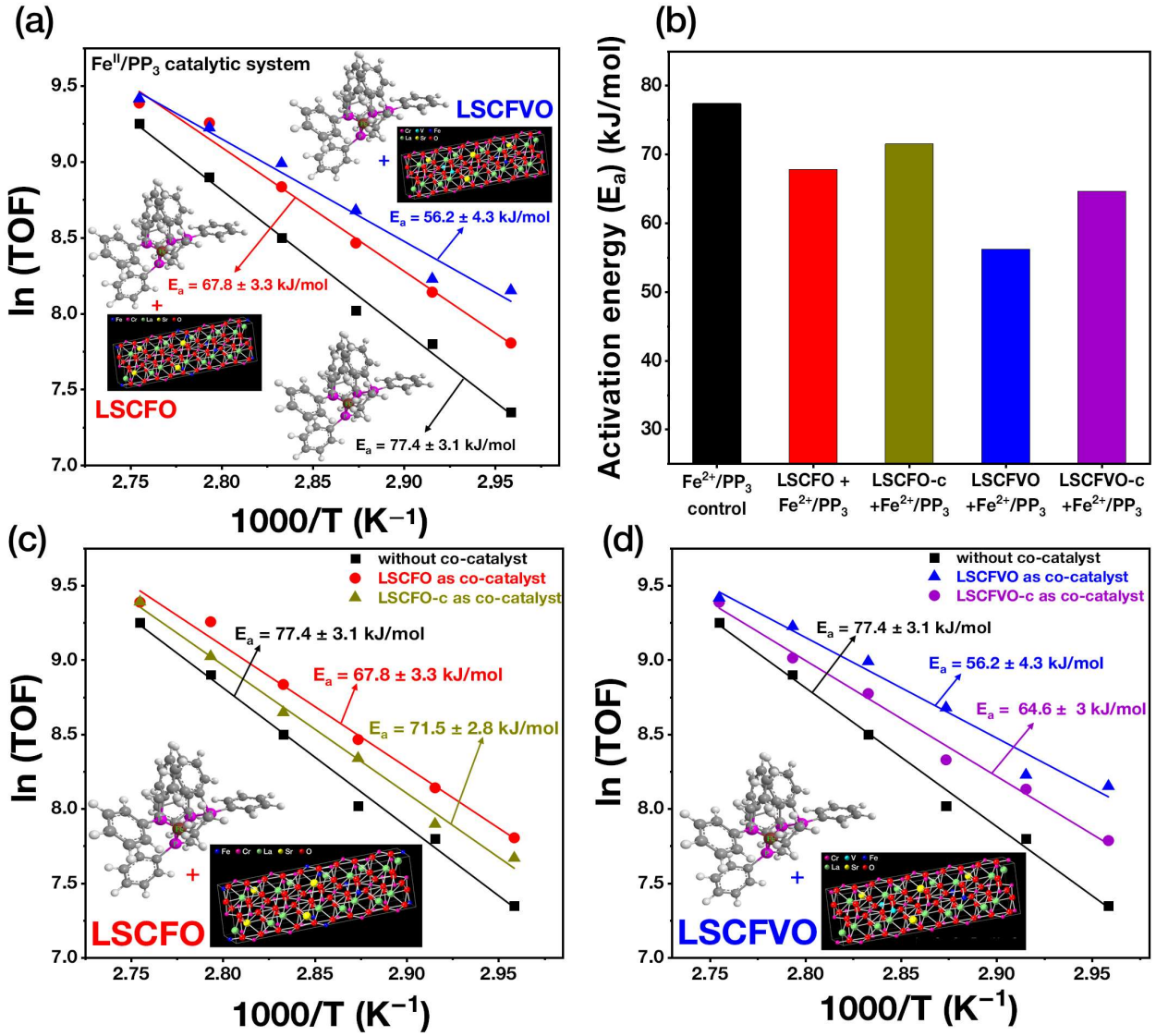


Figure 4. (**a**) Arrhenius plots for the Fe^{2+}/PP_3 catalytic system in the absence (black line) and in the presence of LSCFO (red line) and LSCFVO (blue line), showing reduced activation energies upon addition of the multimetallic perovskite co-catalysts. (**b**) Activation energy values derived from linear fits, demonstrating substantial barrier reductions with both nano-oxides (as prepared and thermally treated). (**c**) Comparison of the co-catalytic behavior of LSCFO (red line) with its calcined form, LSCFO-c (gold-colored line). (**d**) Comparison of the co-catalytic behavior of LSCFVO (blue line) with its calcined form, LSCFVO-c (purple line).

A more pronounced E_a-decrease effect was observed for the vanadium-containing perovskite, LSCFVO (Figure 4a,d, blue line). The as-prepared {LSCFVO + Fe^{2+}/PP_3} catalyst lowered the activation energy to 56.2 ± 4.3 kJ mol^{-1}, representing the largest decrease among all materials tested and corresponding to an approximate $\Delta E_a = -21$ kJ mol^{-1} relative to the Fe^{2+}/PP_3 system operating without a co-catalyst suggesting a stronger interfacial contribution (Figure 5). Upon calcination (LSCFVO-c), the activation energy increased to 64.6 ± 3.0 kJ mol^{-1} (Figure 4d, purple line), consistent with structural relaxation and partial loss of defect-rich surface states upon heating. Nevertheless, the performance of LSCFVO-c remained superior to both the control and the LSCFO-based materials (Figure 4b–d).

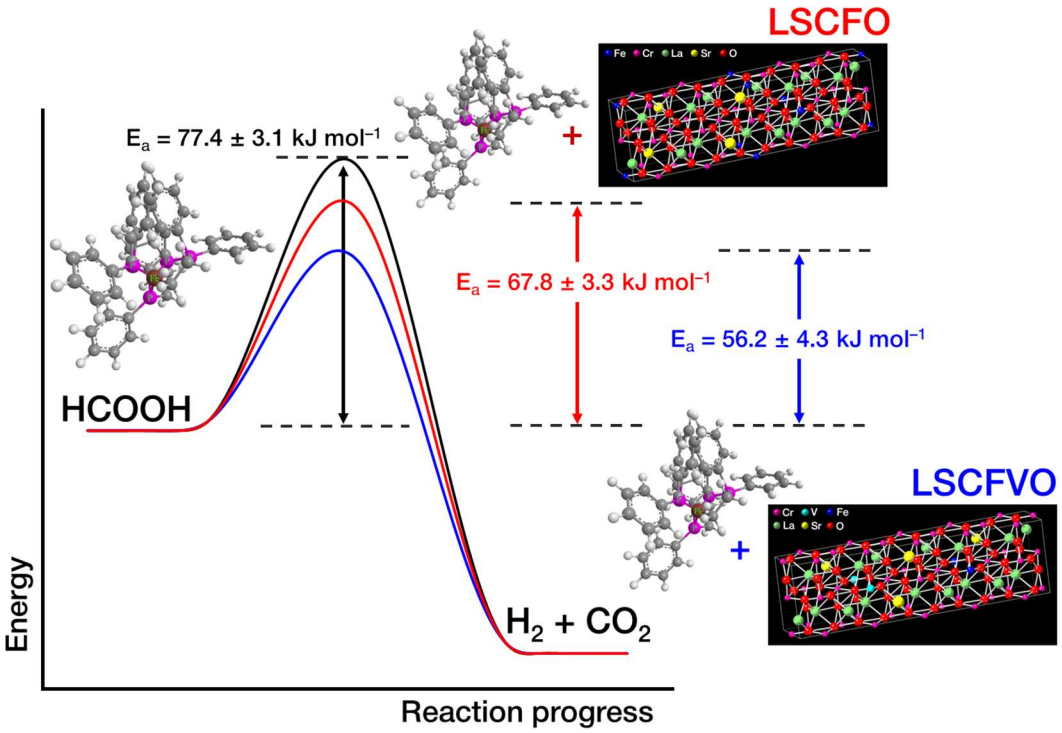


Figure 5. Schematic illustration of the formic acid dehydrogenation pathway and the associated reductions in activation barriers induced by the multimetallic perovskite nano-oxides LSCFO (ΔE_a = –9.6 kJ mol^{-1}) and LSCFVO (ΔE_a = –21.2 kJ mol^{-1}).

Figure 4b presents a comparative bar chart summarizing the activation energies for the catalytic system without a co-catalyst and for those incorporating the as-prepared and thermally treated multimetallic perovskites. These trends highlight the critical influence of perovskite composition, defect structure and intrinsic lattice strain on catalytic enhancement. The superior performance of the as-prepared materials suggests that surface disorder, oxygen vacancies, and labile surface oxygen are likely to play central roles in boosting the FADH catalysis.

In addition, technology-wise, the present results underscore the potential of FSP technology for the synthesis of multimetallic perovskites with controlled surface and microstructural engineering, including defect formation, surface hydroxylation, and lattice strain. This allows one-step engineering of efficient co-catalysts capable of lowering the energetic barriers in homogeneous catalytic systems for hydrogen production from formic acid (see Figure 5).

3. Materials and Methods

3.1. One-Step Multimetallic Perovskite Engineering via Flame Spray Pyrolysis

A flame spray reactor was employed to produce multimetallic {LaSrCrFeO} and {LaSrCrFeVO} perovskites via the flame spray pyrolysis (FSP) method, as schematically illustrated in Figure 6a,c. The specific nominal compositions $La_{0.75}Sr_{0.25}Cr_{0.9}Fe_{0.1}O_{3-\delta}$ and $La_{0.75}Sr_{0.25}Cr_{0.9}Fe_{0.05}V_{0.05}O_{3-\delta}$ (codenamed LSCFO and LSCFVO, correspondingly) were rationally selected to combine structural stability with enhanced redox and electronic functionalities. Partial substitution of La^{3+} by Sr^{2+} (x = 0.25) induces charge imbalance, compensated by oxygen nonstoichiometry (x > 0) that enhances lattice oxygen mobility and redox flexibility. Substitution at the B-site with Fe and Fe/V introduces mixed-valence centers (Fe^{3+}/Fe^{2+} and V^{5+}/V^{4+}). The co-doped Fe–V perovskite was designed to further strengthen redox synergy and optimize the balance between oxygen-vacancy concentra-

tion and electronic conductivity, thereby maximizing co-catalytic efficiency under reaction conditions. To decouple the catalytic roles of the A-site (La–Sr) and B-site (Cr–Fe) components and verify the synergistic effect in the multimetallic perovskites, the single-site doped oxides {LaSrO} and {CrFeO} were also synthesized as controls. In particular, the stoichiometries of the two sites were maintained, namely $La_{0.75}Sr_{0.25}O_{3-\delta}$ (referred to as LSO) and $Cr_{0.9}Fe_{0.1}O_{3-\delta}$ (referred to as CFO). The produced materials are listed in Table 1.

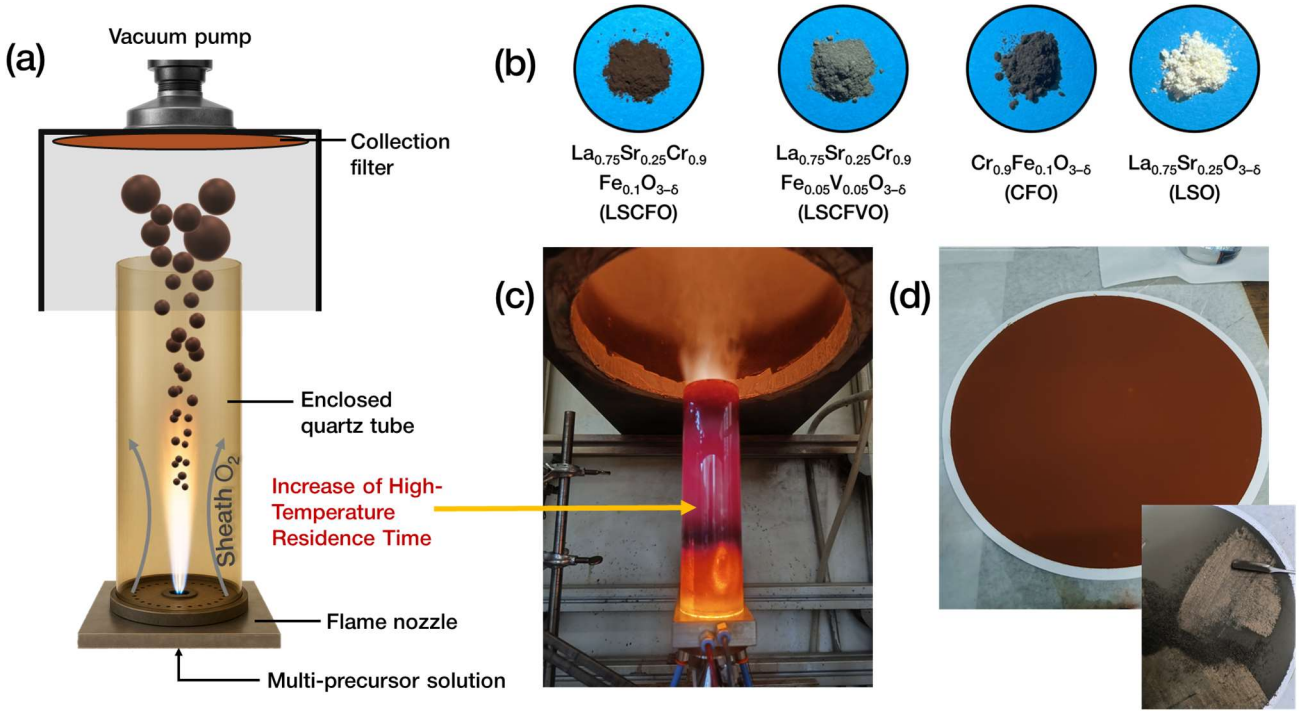


Figure 6. (**a**) Schematic representation of the one-step multimetallic perovskite engineering setup via flame spray pyrolysis (FSP). (**b**) Representative photographs of the as-prepared FSP-derived powders—LSCFO, LSCFVO, CFO and LSO—along with their nominal stoichiometries. (**c**) Photograph of the FSP reactor setup used for the multimetallic perovskite synthesis. The quartz tube was employed to increase high-temperature residence time (HTRT). (**d**) Collection filters after deposition, either fully covered with LSCFO powder or shown during mechanical scraping of the LSCFVO material.

The metal precursor solution for LSCFO was prepared by dissolving 0.25 mol L^{-1} lanthanum(III) nitrate hexahydrate (Thermo Fisher Scientific, Waltham, MA, USA, 99.9% purity) and 0.033 mol L^{-1} iron(III) nitrate nonahydrate (Sigma-Aldrich, St. Louis, MO, USA, >99% purity) in ethanol; 0.083 mol L^{-1} strontium acetate (Strem Chemicals Inc., Newburyport, MA, USA) in acetic acid; and 0.3 mol L^{-1} chromium(III) acetylacetonate (Sigma-Aldrich, St. Louis, MO, USA, >99% purity) in xylene. The solvent ratio was ethanol: acetic acid: xylene = 3.5:1.5:3, and the solutions were then combined to obtain the final precursor mixture. Regarding the LSCFVO material, 0.25 mol L^{-1} lanthanum(III) nitrate hexahydrate and 0.017 mol L^{-1} iron(III) nitrate nonahydrate were dissolved in ethanol; 0.083 mol L^{-1} strontium acetate in acetic acid; 0.3 mol L^{-1} chromium(III) acetylacetonate and 0.017 mol L^{-1} vanadium(V) oxytriisopropoxide (Tokyo Chemical Industry Co., Ltd., Chuo-ku, Tokyo, Japan, purity >97%) in xylene.

For the LSO material, 0.167 mol L^{-1} lanthanum(III) nitrate hexahydrate and 0.056 mol L^{-1} strontium acetate were solubilized in ethanol and water, respectively. For the CFO material, in turn, 0.2 mol L^{-1} chromium(III) acetylacetonate and 0.022 mol L^{-1} iron(III)

acetylacetonate (Sigma-Aldrich, St. Louis, MO, USA, >99% purity) were dissolved in a mixture of acetic acid and xylene.

The precursor solutions were delivered through a capillary at a flow rate of 5 mL min^{-1} and dispersed with oxygen (O_2, Linde, Dublin, Ireland, purity > 99%) at 5 L min^{-1} into a stoichiometric, self-sustained oxygen–methane pilot flame (O_2: 4 L min^{-1}, CH_4: 2 L min^{-1}) to initiate combustion. A pressure drop of 2 bar was maintained at the nozzle tip, while an additional 10 L min^{-1} of sheath O_2 was supplied to stabilize the flame. A key challenge of this synthesis is the complete and homogeneous incorporation of all metal cations into a single, well-ordered perovskite lattice. To achieve stabilization of the multimetal-oxide perovskite, high-temperature residence time (HTRT) of the particles is required. From a thermodynamic perspective, the elevated flame temperature and prolonged particle residence time in the FSP environment provide the driving force for complete cation interdiffusion and lattice equilibration, thus promoting the progression of the system toward Gibbs free energy minimization.

For this reason, solvents with high standard enthalpies of combustion are employed, such as xylene ($\Delta_c H^{\varnothing}_{298} = -4550$ kJ mol^{-1}), ethanol ($\Delta_c H^{\varnothing}_{298} = -1376$ kJ mol^{-1}), and acetic acid ($\Delta_c H^{\varnothing}_{298} = -875$ kJ mol^{-1}) [85,86]. Among these, xylene exhibits the highest combustion enthalpy, providing the most exothermic flame environment and thereby promoting higher flame temperatures and more complete precursor decomposition during FSP. Consequently, the FSP flame was confined within a 20 cm-long quartz tube (Figure 6a), hermetically sealed at the burner to further enhance the HTRT.

Post-FSP Thermal Treatment

The flame spray pyrolysis (FSP) synthesis pathway induces intrinsic lattice strain throughout the multimetallic perovskite nanoparticles, an Feature arising from the rapid heating and quenching inherent to FSP [55,56]. This strain stabilizes the anchored metal sites within the lattice and may modify the electronic structure and surface energy, probably affecting HCOOH dehydrogenation.

To test this hypothesis, the LSCFO and LSCFVO materials were subjected to a mild post-synthesis thermal treatment designed to relax the lattice (hereafter denoted LSCFO-c and LSCFVO-c, where "c" indicates calcination). A calcination protocol of 400 °C for 2 h in air was carefully chosen to dissipate lattice strain while preserving the perovskite crystallite size (Figure S8), ensuring that no additional structural variables confounded the evaluation of their catalytic behavior.

3.2. Characterization of Multimetallic Perovskites

X-ray Diffraction. X-ray diffraction (XRD) data were acquired at room temperature using a Bruker D8 Advance 2theta diffractometer (Karlsruhe, Germany) equipped with copper radiation (Cu Kα, λ = 1.5406 Å) and a secondary monochromator (operating at 36 kV, 36 mA). Measurements were conducted over the 2θ range from 10° to 80°. Crystal size was determined using the Scherrer formula (Equation (3)) [87],

$$d_{XRD} = \frac{K\,\lambda}{FWHM \times \cos\theta} \quad (3)$$

where K = 0.9, and FWHM represents the full width at half-maximum of the XRD peaks. The XRD patterns were recorded in standard Bragg-Brentano geometry using a step-scanning mode with a step size of 0.003° and a counting time of 1 s/step.

Raman Spectroscopy. Raman spectra were recorded with a HORIBA XploRA PLUS Raman microscope (HORIBA Scientific, Kyoto, Japan) coupled to an Olympus BX41 microscope (Kyoto, Japan), equipped with a 785 nm diode laser as the excitation source focused

with a microscope. The spectra were measured with following conditions: for 10 s with 30 accumulations with a laser intensity of 10 mW.

N_2 Porosimetry. The N_2 adsorption−desorption isotherms were measured at 77 K on a NOVAtouch LX^2 Quantachrome porosimeter (Boynton Beach, FL, USA). Prior to the measurements, the samples were degassed at 80 °C for 16 h under a vacuum. The specific surface area (SSA) was determined using the Brunauer−Emmett−Teller (BET) method for adsorption and desorption data points. The specific surface area was found using adsorption data points in the relative pressure P/P_0 range of 0.1−0.3. Pore-size analysis was performed using the Density Functional Theory (DFT) model, based on adsorption data collected within the 0.35–0.99 P/P_0 range, while the total pore volume was obtained from the adsorption points at P/P_0 = 0.99.

Thermogravimetric Analysis (TG-TDA). The thermal profile of multimetallic perovskites was studied by thermogravimetric (TGA) analysis performed using a DTG-60 instrument (SHIMADZU, Kyoto, Japan) and the analyzer TA-60 WS (SHIMADZU, Kyoto, Japan). In all measurements, approximately 50 mg of material was used and placed in a platinum capsule on one arm of the thermocouple. An empty platinum capsule was also used as a reference in the other arm. Finally, the measurements were made at a temperature range of 20 to 900 °C, at a rate of 5 °C min^{-1}, under synthetic air flow.

X-Ray Fluorescence (XRF). The actual metal stoichiometric percentages were determined using the M6-Jetstream scanner (Bruker Nano GmbH, Berlin, Germany), which is equipped with a 30 W Rhodium anode X-ray tube, polycapillary optics, and a silicon drift detector (active area: 30 mm^2). The polycapillary full lens focuses the X-ray radiation from the tube on the target. The X-ray tube was operated at 50 kV and 600 µA voltage with the use of Ti 200 µm Al 200 µm filter. The measuring head was positioned at the focal point of the M6 Jetstream camera, aiming for a nominal beam spot of 100 µm for Mo Kα. The collected spectra were processed and visualized with the built-in M6-Jetstream ESPRIT software (version 1.6.621.0).

3.3. Catalytic HCOOH/H_2 Production Process

Catalytic experiments were conducted under argon in double-walled, thermostated glass vessel with magnetic stirring. For each run, a propylene carbonate/formic acid (PC/FA) mixture (4:2 *v*/*v*) was preheated at 80 ± 2 °C for 30 min under continuous agitation. Fe^{2+} precursor ($Fe(BF_4)_2 \cdot 6H_2O$, 2.5 mg, 7.5 µmol) was then introduced into 6 mL of the PC/FA mixture, followed by addition of 5 mg of tris(2-(diphenylphosphino)ethyl)phosphine (PP_3), establishing an Fe:ligand (1:1) ratio. The catalytic reaction initiated immediately upon mixing. After 5 min of reaction, a controlled amount of multimetallic nano-oxide nanoparticles, previously ultrasonically dispersed in 1 mL of PC, was introduced into the system, serving as co-catalyst. Gas evolution was monitored using an automatic gas burette, and the total gas volume was recorded throughout the reaction at 10-min intervals following co-catalyst addition. All catalytic experiments were conducted as 2 mL batch formic acid reactions, using the Fe^{2+}/PP_3 system, with or without multimetallic perovskite co-catalysts, under otherwise identical conditions. Gas evolution was monitored until equilibrium was reached, corresponding to the theoretical maximum gas volume of approximately 2.4 L. Moreover, they were conducted at ambient pressure, and each measurement was repeated at least twice to verify the reproducibility of the results. The reactor was also coupled to a GC–TCD system (Shimadzu GC-2014 gas chromatograph equipped with a thermal conductivity detector, a Carboxen-1000 column, and Ar as the carrier gas) to quantify and analyze the generated gases. GC analysis (see Figure S9 in Supporting Information) showed that the evolved gases consisted exclusively of H_2 and CO_2 in a 1:1 ratio, with no detectable carbon monoxide (CO), in agreement

with previous reports [16,17,20]. Each molecule of formic acid, via the dehydrogenation pathway, produces 1 mol of H_2 and 1 mol of CO_2. Catalytic turnover numbers (TONs) were calculated as the number of moles of products (H_2 and CO_2) formed during the reaction per mole of the molecular Fe^{2+} catalyst [9,19,21], explicitly excluding Fe atoms present in the multimetallic nano-oxides, according to

$$\mathrm{TONs} = \frac{\mathrm{V_{H_2+CO_2}} / \left(\mathrm{V_{m,H_2}} + \mathrm{V_{m,CO_2}}\right)}{\mathrm{n_{Fe}}} \quad (4)$$

where V_{H_2} and V_{CO_2} are the volumes of produced H_2 and CO_2 gases, respectively. V_{m,H_2} (=24.49 L mol^{-1}) and V_{m,CO_2} (=24.42 L mol^{-1}) are the molar volumes of corresponding gases at measurement conditions and n_{Fe} are the moles of Fe^{2+} catalyst precursor {$Fe(BF_4)_2 \cdot 6H_2O$} added. Turnover frequencies (TOFs) were obtained by dividing TON values by the reaction time (t) at equilibrium (expressed in hours), as shown in

$$\mathrm{TOFs} = \frac{\mathrm{TONs}}{\mathrm{t\ (h)}} \quad (5)$$

In Equation (5), the reaction time corresponds to the time required to reach catalytic equilibrium, defined experimentally as the point at which no further increase in the total evolved gas volume is observed within experimental error. This time was determined directly from the gas evolution profiles for each experiment and was used to normalize the corresponding TON values.

3.4. Solution Potential (E_h) Monitoring

The solution potential (E_h) of the reaction medium was monitored in-situ throughout the catalytic procedure using an ORP electrode (HANNA, Smithfield, RI, USA, HI36180) equipped with a Pt ring and calibrated against the Standard Hydrogen Electrode (SHE). The electrode was inserted directly into the reactor. During catalytic experiments performed under identical conditions, E_h was continuously recorded. Measurements were taken after the addition of each reagent and subsequently at 10-min intervals under continuous stirring at 80 ± 2 °C. To determine the redox potential of the multimetallic perovskite-type nano-oxides in propylene carbonate and to assess their potential contribution upon introduction into the reaction medium, we measured their potential prior to addition. The particles were dispersed in PC at a concentration that mimics their catalytic use, namely 20 mg in 2 mL of solvent for the redox measurements (corresponding to 10 mg in 1 mL used for dispersion in the catalytic experiments).

3.5. Arrhenius Analysis

A total of 7.5 μmol of $Fe(BF_4)_2 \cdot 6H_2O$ was dispersed in a PC/FA mixture (4:2 *v*/*v*), followed by the addition of 7.5 μmol of $P(CH_2CH_2PPh_2)_3$. The reaction mixture was then supplemented with 10 mg of multimetallic perovskite co-catalyst, previously dispersed in 1 mL of propylene carbonate. The reaction temperature was controlled within the range of 65–90 °C. The activation energy was calculated from the Arrhenius relationship (Equation (6))

$$\ln(\mathrm{TOF}) = -\frac{\mathrm{E_a}}{\mathrm{R}}\left(\frac{1}{\mathrm{T}}\right) + \mathrm{C} \quad (6)$$

where E_a is the activation energy in kJ mol^{-1}, T is the temperature in K, R is the universal gas constant (8.314 J mol^{-1} K^{-1}), and C is the constant obtained from the linear regression.

4. Conclusions

In this work, we demonstrated that multimetallic perovskite-type nano-oxides synthesized by flame spray pyrolysis (FSP) technology—namely {LaSrCrFeO} and {LaSrCrFeVO}—act as efficient co-catalysts for hydrogen production from formic acid using the Fe^{2+}/PP_3 molecular system. Structural characterization confirmed the formation of single-phase, compositionally complex perovskites with nanoscale crystallite sizes (65–75 nm), lattice strain, and defect-rich surfaces generated by the far-from-equilibrium conditions of FSP. Raman spectroscopy further verified their mixed A- and B-site coordination environments and the presence of defect-activated vibrational modes, consistent with oxygen non-stoichiometry and cationic disorder.

Catalytic tests revealed that both LSCFO and LSCFVO markedly enhance the H_2 evolution rates compared with the Fe^{2+}/PP_3 system alone. The co-catalysts accelerated significantly the H_2/FADH by >200% and increased the initial TOFs by ~300%. Solution redox potential (E_h) monitoring provided mechanistic insight into these enhancements: the multimetallic perovskites stabilized significantly more reducing environments (−70 to −90 mV), which favor the formation of Fe–hydride intermediates involved in the rate-determining step of formic acid dehydrogenation. Consistent with literature reports, such sustained reducing E_h values reflect the ability of the system to facilitate key elementary steps required for efficient FADH catalysis. Importantly, these effects were not observed for the parent oxides (LSO and CFO), highlighting that the co-catalytic behavior arises from the multimetallic perovskite lattice, rather than from single-site oxide components.

Arrhenius analysis confirmed the thermodynamic origin of the catalytic promotion. The activation energy of the reaction by Fe^{2+}/PP_3 (77.4 ± 3.1 kJ mol^{-1}) decreased to 67.8 ± 3.3 kJ mol^{-1} in the presence of LSCFO and further to 56.2 ± 4.3 kJ mol^{-1} with LSCFVO, demonstrating that these MEOs effectively lower the barrier of rate-determining step of the reaction, consistent with facilitated Fe–hydride formation along the catalytic pathway. Calcination at 400 °C slightly attenuated but did not eliminate the co-catalytic enhancement, indicating that strain-stabilized and defect-rich surface states—partially relaxed upon heating—play a central role in mediating the interaction between the perovskite surface and the catalytic components.

Overall, this study establishes FSP-generated multimetallic perovskites as a robust and versatile platform for co-catalytic enhancement of homogeneous H_2 production catalyst from formic acid. From a technological standpoint, FSP provides a scalable, single-step route toward industrially relevant co-catalysts for LOHC-based hydrogen release. The generality of the approach suggests broad applicability in other molecular catalytic systems where base-acid and/or redox-active oxide interfaces can accelerate thermally activated steps.

Supplementary Materials: The following supporting information can be downloaded at: https://www.mdpi.com/article/10.3390/catal16010044/s1, Figure S1: (a) Photographs of the LSCFO, LSCFVO, CFO, and LSO samples positioned in the sample holder, indicating the area from which the XRF signal was collected. (b) XRF spectra of the LSCFO, LSCFVO, CFO, and LSO materials, showing the quantitative detection of all constituent elements in each composition. (c) Comparative XRF spectra of the LSCFO and LSCFVO perovskites in a magnified region, highlighting the appearance of the vanadium V Kα emission line and the resulting broadening of the overall spectral envelope. Figure S2: (a–d) N_2 adsorption-desorption isotherms of LSCFO, LSCFVO, CFO and LSO materials. Figure S3: Thermogravimetric analysis of multimetallic perovskites (a) LSCFO and (b) LSCFVO. Figure S4: XRF spectra of the Cl-LSO material shown in (a) a broad energy range, displaying the characteristic La and Sr emission lines, and (b) a magnified low-energy region, where the Cl Kα signal is resolved and quantified at approximately 21%. Figure S5: (a) Volume of gases (H_2 + CO_2) evolved by the {Fe^{2+}/PP_3} catalytic system in the absence (black line) and in the presence of (a) Cl-LSO (orange line);

inset: initial TOFs and turnover numbers of the Fe^{2+}/PP_3 system with or without co-catalyst Cl-LSO addition during FADH. (b) Comparative Eh profiles of {Fe^{2+}/PP_3} control (black bars) and {Cl-LSO + Fe^{2+}/PP_3} (orange bars). Figure S6: Gas production rate vs. mass of (a) LSCFO and (b) LSCFVO multimetallic perovskite oxides, serving as co-catalysts in FADH, using {Fe^{2+}/PP_3} molecular catalyst. Figure S7: Comparative E_h profiles of {Fe^{2+}/PP_3} control (black bars) and multimetallic perovskites (a) {LSCFO + Fe^{2+}/PP_3} (red bars), {LSCFO-c + Fe^{2+}/PP_3} (gold-colored bars) and (b) {LSCFVO + Fe^{2+}/PP_3} (blue bars), {LSCFVO-c + Fe^{2+}/PP_3} (purple bars); insets: Volume of gases (H_2 + CO_2) evolved by the {Fe^{2+}/PP_3} catalytic system in the absence (black line) and in the presence of (a) LSCFO (red line) and LSCFO-c (gold-colored line) and (b) LSCFVO (blue line) and LSCFVO-c (purple line). Figure S8: XRD patterns of the multimetallic perovskites LSCFO and LSCFVO, both as-prepared and after calcination at 400 °C for 2 h (denoted as LSCFO-c and LSCFVO-c, respectively). The XRD profiles after calcination confirm the structural stability of the materials, showing no detectable change in crystallite size. Figure S9: Representative GC spectrum acquired during the catalytic reaction for the {LSCFVO + Fe^{2+}/PP_3} system, demonstrating that the evolved gases consisted exclusively of H_2 and CO_2 in a 1:1 ratio, with no detectable carbon monoxide (CO). Table S1: XRF data for the studied multimetallic perovskites and single-site doped oxides. Table S2: Raman mode vibrations of multimetallic perovskites LSCFO, LSCFVO and single-site doped oxides LSO, CFO.

Author Contributions: Materials synthesis, C.D.; catalytic experiments, K.G.; XRF measurements, A.A. and D.F.A.; investigation, C.D. and K.G.; writing—original draft preparation, C.D. and K.G.; writing—review and editing, C.D., K.G., M.L. and Y.D.; conceptualization, M.L. and Y.D.; supervision, M.L. and Y.D. All authors have read and agreed to the published version of the manuscript.

Funding: The research project is implemented in the framework of Hellenic Foundation for Research & Innovation (H.F.R.I.) call "Basic Research Financing (Horizontal support for all sciences)" under the National Recovery and Resilience Plan "Greece 2.0" funded by the European Union—Next Generation EU (H.F.R.I. Project Number: 16283–ECOS).

Data Availability Statement: The original contributions presented in this study are included in the article/Supplementary Materials. Further inquiries can be directed to the corresponding authors.

Acknowledgments: The authors acknowledge the Hellenic Foundation for Research & Innovation (H.F.R.I) and the National Recovery and Resilience Plan *(Greece 2.0)*, funded by the European Union—*NextGenerationEU*, for financial support.

Conflicts of Interest: The authors declare no conflicts of interest.

References

1. Eppinger, J.; Huang, K.-W. Formic Acid as a Hydrogen Energy Carrier. *ACS Energy Lett.* **2017**, *2*, 188–195. [CrossRef]
2. Falcone, P.M.; Hiete, M.; Sapio, A. Hydrogen Economy and Sustainable Development Goals: Review and Policy Insights. *Curr. Opin. Green Sustain. Chem.* **2021**, *31*, 100506. [CrossRef]
3. Modisha, P.M.; Ouma, C.N.M.; Garidzirai, R.; Wasserscheid, P.; Bessarabov, D. The Prospect of Hydrogen Storage Using Liquid Organic Hydrogen Carriers. *Energy Fuels* **2019**, *33*, 2778–2796. [CrossRef]
4. Hren, R.; Vujanović, A.; Van Fan, Y.; Klemeš, J.J.; Krajnc, D.; Čuček, L. Hydrogen Production, Storage and Transport for Renewable Energy and Chemicals: An Environmental Footprint Assessment. *Renew. Sustain. Energy Rev.* **2023**, *173*, 113113. [CrossRef]
5. Valentini, F.; Marrocchi, A.; Vaccaro, L. Liquid Organic Hydrogen Carriers (LOHCs) as H-Source for Bio-Derived Fuels and Additives Production. *Adv. Energy Mater.* **2022**, *12*, 2103362. [CrossRef]
6. Boddien, A.; Loges, B.; Gärtner, F.; Torborg, C.; Fumino, K.; Junge, H.; Ludwig, R.; Beller, M. Iron-Catalyzed Hydrogen Production from Formic Acid. *J. Am. Chem. Soc.* **2010**, *132*, 8924–8934. [CrossRef]
7. Wang, Z.; Qian, J.; Sun, Z.; Zhang, Z.; He, M.; Chen, Q. Application of Heterogeneous Catalysis in Formic Acid-Based Hydrogen Cycle System. *Catalysts* **2023**, *13*, 1168. [CrossRef]
8. Kumar, N.S.; Adhikary, A. Transition Metal Pincer Catalysts for Formic Acid Dehydrogenation: A Mechanistic Perspective. *Front. Chem.* **2024**, *12*, 1452408. [CrossRef]
9. Boddien, A.; Mellmann, D.; Gärtner, F.; Jackstell, R.; Junge, H.; Dyson, P.J.; Laurenczy, G.; Ludwig, R.; Beller, M. Efficient Dehydrogenation of Formic Acid Using an Iron Catalyst. *Science* **2011**, *333*, 1733–1736. [CrossRef]

10. Gkatziouras, C.; Solakidou, M.; Louloudi, M. Efficient [Fe-Imidazole@SiO_2] Nanohybrids for Catalytic H_2 Production from Formic Acid. *Nanomaterials* **2023**, *13*, 1670. [CrossRef]
11. Theodorakopoulos, M.; Solakidou, M.; Deligiannakis, Y.; Louloudi, M. Double-Ligand [Fe/PNP/PP3] and Their Hybrids [Fe/SiO_2@PNP/PP3] as Catalysts for H_2-Production from HCOOH. *Energies* **2024**, *17*, 3934. [CrossRef]
12. Gravvani, K.; Solakidou, M.; Louloudi, M. Highly-Efficient Reusable [Silica@Iminophosphine-Fe^{II}] Hybrids for Hydrogen Production via Formic Acid and Formaldehyde Dehydrogenation. *Chem. A Eur. J* **2025**, *31*, e202404440. [CrossRef]
13. Sotiriou, A.; Aspri, E.; Deligiannakis, Y.; Louloudi, M. Engineering of Hybrid SiO_2@{N-P-Fe} Catalysts with Double-Ligand for Efficient H_2 Production from HCOOH. *Energies* **2025**, *18*, 514. [CrossRef]
14. Gkatziouras, C.; Solakidou, M.; Louloudi, M. Formic Acid Dehydrogenation over a Recyclable and Self-Reconstructing Fe/Activated Carbon Catalyst. *Energy Fuels* **2024**, *38*, 17914–17926. [CrossRef]
15. Gkatziouras, C.; Dimitriou, C.; Smykała, S.; Deligiannakis, Y.; Louloudi, M. {Fe^{2+} –Imidazole} Catalyst Grafted on Magnetic {Fe@Graphitized C} Nanoparticles: A Robust Hybrid–Catalyst for H_2 Production from HCOOH. *J. Mater. Chem. A* **2025**, *13*, 21659–21671. [CrossRef]
16. Stathi, P.; Deligiannakis, Y.; Avgouropoulos, G.; Louloudi, M. Efficient H_2 Production from Formic Acid by a Supported Iron Catalyst on Silica. *Appl. Catal. A Gen.* **2015**, *498*, 176–184. [CrossRef]
17. Stathi, P.; Deligiannakis, Y.; Louloudi, M. Co-Catalytic Enhancement of H_2 Production by SiO_2 Nanoparticles. *Catal. Today* **2015**, *242*, 146–152. [CrossRef]
18. Stathi, P.; Deligiannakis, Y.; Louloudi, M. Co-Catalytic Effect of Functionalized SiO_2 Materials on H_2 Production from Formic Acid by an Iron Catalyst. *MRS Proc.* **2014**, *1641*, mrsf13-1641-aa06-26. [CrossRef]
19. Solakidou, M.; Deligiannakis, Y.; Louloudi, M. Heterogeneous Amino-Functionalized Particles Boost Hydrogen Production from Formic Acid by a Ruthenium Complex. *Int. J. Hydrogen Energy* **2018**, *43*, 21386–21397. [CrossRef]
20. Solakidou, M.; Theodorakopoulos, M.; Deligiannakis, Y.; Louloudi, M. Double-Ligand Fe, Ru Catalysts: A Novel Route for Enhanced H_2 Production from Formic Acid. *Int. J. Hydrogen Energy* **2020**, *45*, 17367–17377. [CrossRef]
21. Gemenetzi, A.; Deligiannakis, Y.; Louloudi, M. Controlled Photoplasmonic Enhancement of H_2 Production via Formic Acid Dehydrogenation by a Molecular Fe Catalyst. *ACS Catal.* **2023**, *13*, 9905–9917. [CrossRef]
22. Theodorakopoulos, M.; Deligiannakis, Y.; Louloudi, M. Solution-Potential and Solution-Hydrides as Key-Parameters in H_2 Production via HCOOH-Dehydrogenation by Fe- and Ru-Molecular Catalysts. *Int. J. Hydrogen Energy* **2024**, *58*, 1608–1617. [CrossRef]
23. Polo-Garzon, F.; Wu, Z. Acid–Base Catalysis over Perovskites: A Review. *J. Mater. Chem. A* **2018**, *6*, 2877–2894. [CrossRef]
24. Chang, H.; Bjørgum, E.; Mihai, O.; Yang, J.; Lein, H.L.; Grande, T.; Raaen, S.; Zhu, Y.-A.; Holmen, A.; Chen, D. Effects of Oxygen Mobility in La–Fe-Based Perovskites on the Catalytic Activity and Selectivity of Methane Oxidation. *ACS Catal.* **2020**, *10*, 3707–3719. [CrossRef]
25. Voorhoeve, R.J.H.; Johnson, D.W.; Remeika, J.P.; Gallagher, P.K. Perovskite Oxides: Materials Science in Catalysis. *Science* **1977**, *195*, 827–833. [CrossRef]
26. Tasleem, S.; Tahir, M. Recent Progress in Structural Development and Band Engineering of Perovskites Materials for Photocatalytic Solar Hydrogen Production: A Review. *Int. J. Hydrogen Energy* **2020**, *45*, 19078–19111. [CrossRef]
27. Hwang, J.; Rao, R.R.; Giordano, L.; Katayama, Y.; Yu, Y.; Shao-Horn, Y. Perovskites in Catalysis and Electrocatalysis. *Science* **2017**, *358*, 751–756. [CrossRef]
28. Jun, A.; Kim, J.; Shin, J.; Kim, G. Perovskite as a Cathode Material: A Review of Its Role in Solid-Oxide Fuel Cell Technology. *ChemElectroChem* **2016**, *3*, 511–530. [CrossRef]
29. Kubicek, M.; Bork, A.H.; Rupp, J.L.M. Perovskite Oxides—A Review on a Versatile Material Class for Solar-to-Fuel Conversion Processes. *J. Mater. Chem. A* **2017**, *5*, 11983–12000. [CrossRef]
30. Wang, W.; Tadé, M.O.; Shao, Z. Research Progress of Perovskite Materials in Photocatalysis- and Photovoltaics-Related Energy Conversion and Environmental Treatment. *Chem. Soc. Rev.* **2015**, *44*, 5371–5408. [CrossRef] [PubMed]
31. Karageorgakis, N.I.; Heel, A.; Bieberle-Hütter, A.; Rupp, J.L.M.; Graule, T.; Gauckler, L.J. Flame Spray Deposition of $La_{0.6}Sr_{0.4}CoO_{3-\delta}$ Thin Films: Microstructural Characterization, Electrochemical Performance and Degradation. *J. Power Sources* **2010**, *195*, 8152–8161. [CrossRef]
32. Sarkar, A.; Wang, Q.; Schiele, A.; Chellali, M.R.; Bhattacharya, S.S.; Wang, D.; Brezesinski, T.; Hahn, H.; Velasco, L.; Breitung, B. High-Entropy Oxides: Fundamental Aspects and Electrochemical Properties. *Adv. Mater.* **2019**, *31*, 1806236. [CrossRef]
33. Albedwawi, S.H.; AlJaberi, A.; Haidemenopoulos, G.N.; Polychronopoulou, K. High Entropy Oxides-Exploring a Paradigm of Promising Catalysts: A Review. *Mater. Des.* **2021**, *202*, 109534. [CrossRef]
34. Aamlid, S.S.; Oudah, M.; Rottler, J.; Hallas, A.M. Understanding the Role of Entropy in High Entropy Oxides. *J. Am. Chem. Soc.* **2023**, *145*, 5991–6006. [CrossRef]
35. Miracle, D.B.; Senkov, O.N. A Critical Review of High Entropy Alloys and Related Concepts. *Acta Mater.* **2017**, *122*, 448–511. [CrossRef]

36. Yeh, J.-W.; Chen, S.-K.; Lin, S.-J.; Gan, J.-Y.; Chin, T.-S.; Shun, T.-T.; Tsau, C.-H.; Chang, S.-Y. Nanostructured High-Entropy Alloys with Multiple Principal Elements: Novel Alloy Design Concepts and Outcomes. *Adv. Eng. Mater.* **2004**, *6*, 299–303. [CrossRef]
37. Cantor, B.; Chang, I.T.H.; Knight, P.; Vincent, A.J.B. Microstructural Development in Equiatomic Multicomponent Alloys. *Mater. Sci. Eng. A* **2004**, *375–377*, 213–218. [CrossRef]
38. Rost, C.M.; Sachet, E.; Borman, T.; Moballegh, A.; Dickey, E.C.; Hou, D.; Jones, J.L.; Curtarolo, S.; Maria, J.-P. Entropy-Stabilized Oxides. *Nat. Commun.* **2015**, *6*, 8485. [CrossRef] [PubMed]
39. McCormack, S.J.; Navrotsky, A. Thermodynamics of High Entropy Oxides. *Acta Mater.* **2021**, *202*, 1–21. [CrossRef]
40. Anandkumar, M.; Trofimov, E. Synthesis, Properties, and Applications of High-Entropy Oxide Ceramics: Current Progress and Future Perspectives. *J. Alloys Compd.* **2023**, *960*, 170690. [CrossRef]
41. Wright, A.J.; Luo, J. A Step Forward from High-Entropy Ceramics to Compositionally Complex Ceramics: A New Perspective. *J. Mater. Sci.* **2020**, *55*, 9812–9827. [CrossRef]
42. Brahlek, M.; Gazda, M.; Keppens, V.; Mazza, A.R.; McCormack, S.J.; Mielewczyk-Gryń, A.; Musico, B.; Page, K.; Rost, C.M.; Sinnott, S.B.; et al. What Is in a Name: Defining "High Entropy" Oxides. *APL Mater.* **2022**, *10*, 110902. [CrossRef]
43. Ko, S.-T.; Lee, T.; Qi, J.; Zhang, D.; Peng, W.-T.; Wang, X.; Tsai, W.-C.; Sun, S.; Wang, Z.; Bowman, W.J.; et al. Compositionally Complex Perovskite Oxides: Discovering a New Class of Solid Electrolytes with Interface-Enabled Conductivity Improvements. *Matter* **2023**, *6*, 2395–2418. [CrossRef]
44. Zhang, D.; De Santiago, H.A.; Xu, B.; Liu, C.; Trindell, J.A.; Li, W.; Park, J.; Rodriguez, M.A.; Coker, E.N.; Sugar, J.D.; et al. Compositionally Complex Perovskite Oxides for Solar Thermochemical Water Splitting. *Chem. Mater.* **2023**, *35*, 1901–1915. [CrossRef]
45. Shen, L.; Du, Z.; Zhang, Y.; Dong, X.; Zhao, H. Medium-Entropy Perovskites Sr(FeαTiβCoγMnζ)O_3-δ as Promising Cathodes for Intermediate Temperature Solid Oxide Fuel Cell. *Appl. Catal. B Environ.* **2021**, *295*, 120264. [CrossRef]
46. Liu, Y.; Tuo, P.; Dai, F.-Z.; Yu, Z.; Lai, W.; Ding, Q.; Yan, P.; Gao, J.; Hu, Y.; Hu, Y.; et al. A Highly Deficient Medium-Entropy Perovskite Ceramic for Electromagnetic Interference Shielding under Harsh Environment. *Adv. Mater.* **2024**, *36*, 2400059. [CrossRef]
47. Li, X.; Shi, C.; Zhang, G.; Zheng, G.; Huang, Z.; Shen, X.; Zhou, J.; Chen, T.; Wang, S. A Medium-Entropy Perovskite Oxide $La_{0.7}Sr_{0.3}Co_{0.25}Fe_{0.25}Ni_{0.25}Mn_{0.25}O_{3-\delta}$ as Intermediate Temperature Solid Oxide Fuel Cells Cathode Material. *Ceram. Int.* **2023**, *49*, 30187–30195. [CrossRef]
48. Esquirol, A.; Brandon, N.P.; Kilner, J.A.; Mogensen, M. Electrochemical Characterization of $La_{0.6}Sr_{0.4}Co_{0.2}Fe_{0.8}$ O_3 Cathodes for Intermediate-Temperature SOFCs. *J. Electrochem. Soc.* **2004**, *151*, A1847. [CrossRef]
49. Zhang, Y.-Q.; Li, J.-H.; Sun, Y.-F.; Hua, B.; Luo, J.-L. Highly Active and Redox-Stable Ce-Doped LaSrCrFeO-Based Cathode Catalyst for CO_2 SOECs. *ACS Appl. Mater. Interfaces* **2016**, *8*, 6457–6463. [CrossRef] [PubMed]
50. Zhang, Y.; Xu, Y.; Gan, L. Exsolved Metallic Iron Nanoparticles in Perovskite Cathode to Enhance CO2 Electrolysis. *J. Solid State Electrochem.* **2022**, *26*, 409–417. [CrossRef]
51. Bimpiri, N.; Konstantinidou, A.; Papazisi, K.M.; Balomenou, S.; Tsiplakides, D. Electrochemical Performance of Iron Doped Lanthanum Strontium Chromites as Fuel Electrodes in High Temperature Solid Oxide Cells. *Electrochim. Acta* **2024**, *475*, 143537. [CrossRef]
52. Psathas, P.; Georgiou, Y.; Moularas, C.; Armatas, G.S.; Deligiannakis, Y. Controlled-Phase Synthesis of $Bi_2Fe_4O_9$ & $BiFeO_3$ by Flame Spray Pyrolysis and Their Evaluation as Non-Noble Metal Catalysts for Efficient Reduction of 4-Nitrophenol. *Powder Technol.* **2020**, *368*, 268–277. [CrossRef]
53. Psathas, P.; Moularas, C.; Smykała, S.; Deligiannakis, Y. Highly Crystalline Nanosized $NaTaO_3$/NiO Heterojunctions Engineered by Double-Nozzle Flame Spray Pyrolysis for Solar-to-H_2 Conversion: Toward Industrial-Scale Synthesis. *ACS Appl. Nano Mater.* **2023**, *6*, 2658–2671. [CrossRef]
54. Moularas, C.; Psathas, P.; Deligiannakis, Y. Electron Paramagnetic Resonance Study of Photo-Induced Hole/Electron Pairs in NaTaO3 Nanoparticles. *Chem. Phys. Lett.* **2021**, *782*, 139031. [CrossRef]
55. Li, S.; Bi, W.; Meng, X.; Zhang, Y.; Zhang, D.; Ling, Y.; Zhang, D.; Xiao, S.; Hu, Y.; Wang, M.; et al. Hydrogen-Bond Network Mediated Lattice-Strain Engineering for CO_2-to-CH_4 Selectivity Regulation via Flame Spray Pyrolysis Strategy. *J. Colloid Interface Sci.* **2026**, *703*, 139159. [CrossRef] [PubMed]
56. Luo, L.; Ju, J.; Wu, Y.; Wan, X.; Li, W.; Li, Y.; Jiang, H.; Hu, Y.; Li, C. Lattice-Strain Engineering of High-Entropy-Oxide Nanoparticles: Regulation by Flame Spray Pyrolysis with Ultrafast Quenching. *Adv. Mater.* **2025**, *37*, 2418856. [CrossRef]
57. Dimitriou, C.; Psathas, P.; Solakidou, M.; Deligiannakis, Y. Advanced Flame Spray Pyrolysis (FSP) Technologies for Engineering Multifunctional Nanostructures and Nanodevices. *Nanomaterials* **2023**, *13*, 3006. [CrossRef] [PubMed]
58. Dimitriou, C.; Belles, L.; Boukos, N.; Deligiannakis, Y. {TiO_2/TiO_2(B)} Quantum Dot Hybrids: A Comprehensible Route toward High-Performance [>0.1 Mol Gr–1 h–1] Photocatalytic H_2 Production from H_2O. *ACS Catal.* **2024**, *14*, 17919–17934. [CrossRef]
59. Phakatkar, A.; Saray, M.; Rasul, M.G.; Sorokina, L.; Ritter, T.; Shokuhfar, T.; Shahbazian-Yassar, R. Ultrafast Synthesis of High Entropy Oxide Nanoparticles by Flame Spray Pyrolysis. *Langmuir* **2021**, *37*, 9059–9068. [CrossRef]

60. Dai, Y.; Ju, J.; Luo, L.; Jiang, H.; Hu, Y.; Li, C. Flame Spray Pyrolysis Synthesis of Ultra-Small High-Entropy Alloy-Supported Oxide Nanoparticles for CO_2 Hydrogenation Catalysts. *Small Methods* **2024**, *8*, 2301768. [CrossRef]
61. Zheng, H.; Zhang, Y.; Xu, Z.; Zhou, G.; Zhao, X.; Huang, Z.; Lin, H. One-Step Synthesis of Pt@(CrMnFeCoNi)3O4 High Entropy Oxide Catalysts through Flame Spray Pyrolysis. *J. Energy Inst.* **2024**, *117*, 101804. [CrossRef]
62. Dimitriou, C.; Deligiannakis, Y. Thermoplasmonic Nano–Hybrid Core@Shell Ag@SiO_2 Films Engineered via One–Step Flame Spray Pyrolysis. *Nanomaterials* **2025**, *15*, 743. [CrossRef]
63. Zschornack, G. *Handbook of X-Ray Data*; Springer: Berlin/Heidelberg, Germany, 2006. [CrossRef]
64. Kawazoe, Y.; Kanomata, T.; Note, R. $LaCrO_3$. In *High Pressure Materials Properties: Magnetic Properties of Oxides Under Pressure: A Supplement to Landolt-Börnstein IV/22 Series*; Kawazoe, Y., Kanomata, T., Note, R., Eds.; Springer: Berlin/Heidelberg, Germany, 2023; pp. 467–470. [CrossRef]
65. Hurtig, N.C.; Gysi, A.P.; Smith-Schmitz, S.E.; Harlov, D. Raman Spectroscopic Study of Anhydrous and Hydrous REE Phosphates, Oxides, and Hydroxides. *Dalton Trans.* **2024**, *53*, 9964–9978. [CrossRef]
66. Denning, J.H.; Ross, S.D. The Vibrational Spectra and Structures of Rare Earth Oxides in the A Modification. *J. Phys. C Solid State Phys.* **1972**, *5*, 1123. [CrossRef]
67. Boldish, S.I.; White, W.B. Vibrational Spectra of Crystals with the A-Type Rare Earth Oxide Structure—I. La_2O_3 and Nd_2O_3. *Spectrochim. Acta Part A Mol. Spectrosc.* **1979**, *35*, 1235–1242. [CrossRef]
68. Shim, S.-H.; Duffy, T.S.; Jeanloz, R.; Yoo, C.-S.; Iota, V. Raman Spectroscopy and X-Ray Diffraction of Phase Transitions in Cr_2O_3 to 61 GPa. *Phys. Rev. B* **2004**, *69*, 144107. [CrossRef]
69. Gomes, A.S.O.; Yaghini, N.; Martinelli, A.; Ahlberg, E. A Micro-Raman Spectroscopic Study of $Cr(OH)_3$ and Cr_2O_3 Nanoparticles Obtained by the Hydrothermal Method. *J. Raman Spectrosc.* **2017**, *48*, 1256–1263. [CrossRef]
70. Bhardwaj, P.; Singh, J.; Kumar, R.; Kumar, D.; Verma, V.; Kumar, R. Oxygen Defects Induced Tailored Optical and Magnetic Properties of $FexCr_2-xO_3$ ($0 \leq x \leq 0.1$) Nanoparticles. *Appl. Phys. A* **2022**, *128*, 135. [CrossRef]
71. Weber, M.C.; Kreisel, J.; Thomas, P.A.; Newton, M.; Sardar, K.; Walton, R.I. Phonon Raman Scattering of $RCrO_3$ Perovskites (R=Y, La, Pr, Sm, Gd, Dy, Ho, Yb, Lu). *Phys. Rev. B* **2012**, *85*, 054303. [CrossRef]
72. Bhadram, V.S.; Sen, A.; Sunil, J.; Panda, D.P.; Sundaresan, A.; Narayana, C. Pressure-Driven Evolution of Structural Distortions in $RCrO_3$ Perovskites: The Curious Case of $LaCrO_3$. *Solid State Sci.* **2021**, *119*, 106708. [CrossRef]
73. Iliev, M.N.; Litvinchuk, A.P.; Hadjiev, V.G.; Wang, Y.-Q.; Cmaidalka, J.; Meng, R.-L.; Sun, Y.-Y.; Kolev, N.; Abrashev, M.V. Raman Spectroscopy of Low-Temperature (Pnma) and High-Temperature (R3c) Phases of $LaCrO_3$. *Phys. Rev. B* **2006**, *74*, 214301. [CrossRef]
74. Kumar, R.; Singh, K.D.; Kumar, R. Effect of Sr Substitution on Structural Properties of $LaCrO_3$ Perovskite. *J. Mater. Sci. Mater. Electron.* **2022**, *33*, 12039–12052. [CrossRef]
75. Singh, K.D.; Pandit, R.; Kumar, R. Effect of Rare Earth Ions on Structural and Optical Properties of Specific Perovskite Orthochromates; $RCrO_3$ (R = La, Nd, Eu, Gd, Dy, and Y). *Solid State Sci.* **2018**, *85*, 70–75. [CrossRef]
76. Scheuermann, W.; Ritter, G.J. The Vibrational Spectra of Strontium Chromate ($SrCrO_4$) and Lead Chromate ($PbCrO_4$). *Z. Für. Naturforschung A* **1970**, *25*, 1856–1862. [CrossRef]
77. Tompsett, G.A.; Sammes, N.M. Characterisation of the SOFC Material, $LaCrO_3$, Using Vibrational Spectroscopy. *J. Power Sources* **2004**, *130*, 1–7. [CrossRef]
78. Vrejoiu, I.; Himcinschi, C.; Jin, L.; Jia, C.-L.; Raab, N.; Engelmayer, J.; Waser, R.; Dittmann, R.; van Loosdrecht, P.H.M. Probing Orbital Ordering in $LaVO_3$ Epitaxial Films by Raman Scattering. *APL Mater.* **2016**, *4*, 046103. [CrossRef]
79. Miyasaka, S.; Fujioka, J.; Iwama, M.; Okimoto, Y.; Tokura, Y. Raman Study of Spin and Orbital Order and Excitations in Perovskite-Type RVO3 (R = La, Nd, and Y). *Phys. Rev. B* **2006**, *73*, 224436. [CrossRef]
80. Frost, R.L.; Palmer, S.J.; Čejka, J.; Sejkora, J.; Plášil, J.; Bahfenne, S.; Keeffe, E.C. A Raman Spectroscopic Study of the Different Vanadate Groups in Solid-State Compounds—Model Case: Mineral Phases Vésigniéite [$BaCu_3(VO_4)_2(OH)_2$] and Volborthite [$Cu_3V_2O_7(OH)_2 \cdot 2H_2O$]. *J. Raman Spectrosc.* **2011**, *42*, 1701–1710. [CrossRef]
81. Sultan, K.; Samad, R.; Najar, F.A.; Abass, S.; Jahan, S.; Rashid Rather, M.; Ikram, M. Structural, Optical and Dielectric Properties of Sr Doped $LaVO_4$. *Adv. Mater. Lett.* **2021**, *12*, 1–6. [CrossRef]
82. Dua, H.; Shukla, R.; Dhaka, R.S. Structural Phase Transition and Its Consequences for the Optical Behavior of $LaV_{1-x}Nb_xO_4$. *Phys. Rev. B* **2021**, *103*, 174107. [CrossRef]
83. Makhlouf, S.A.; Bakr, Z.H.; Al-Attar, H.; Moustafa, M.S. Structural, Morphological and Electrical Properties of Cr_2O_3 Nanoparticles. *Mater. Sci. Eng. B* **2013**, *178*, 337–343. [CrossRef]
84. Smiljanić, S.; Karamanova, E.; Grujić, S.; Rogan, J.; Stojanović, J.; Matijašević, S.; Karamanov, A. Sintering, Crystallization and Foaming of $La_2O_3 \cdot Sr\ 5B_2O_3$ Glass Powders—Effect of the Holding Temperature and the Heating Rate. *J. Non-Cryst. Solids* **2018**, *481*, 375–382. [CrossRef]
85. Haynes, W.M. *CRC Handbook of Chemistry and Physics*, 97th ed.; CRC Press: Boca Raton, FL, USA, 2017.

86. Steele, W.V.; Chirico, R.D.; Cowell, A.B.; Knipmeyer, S.E.; Nguyen, A. Thermodynamic Properties and Ideal-Gas Enthalpies of Formation for 2-Aminoisobutyric Acid (2-Methylalanine), Acetic Acid, (Z)-5-Ethylidene-2-Norbornene, Mesityl Oxide (4-Methyl-3-Penten-2-One), 4-Methylpent-1-Ene, 2,2′-Bis(Phenylthio)Propane, and Glycidyl Phenyl Ether (1,2-Epoxy-3-Phenoxypropane). *J. Chem. Eng. Data* **1997**, *42*, 1053–1066. [CrossRef]
87. Patterson, A.L. The Scherrer Formula for X-Ray Particle Size Determination. *Phys. Rev.* **1939**, *56*, 978–982. [CrossRef]

Disclaimer/Publisher's Note: The statements, opinions and data contained in all publications are solely those of the individual author(s) and contributor(s) and not of MDPI and/or the editor(s). MDPI and/or the editor(s) disclaim responsibility for any injury to people or property resulting from any ideas, methods, instructions or products referred to in the content.